Structural, redox and isotopic behaviors of iron in geological silicate glasses: A NRIXS study of Lamb-Mössbauer factors and force constants

Mathieu Roskosz, Nicolas Dauphas, Justin Hu, Michael Hu, Daniel R. Neuville, Dennis Brown, Wenli Bi, Nicole Nie, Jiyong Zhao, Esen Alp

▶ **To cite this version:**

Mathieu Roskosz, Nicolas Dauphas, Justin Hu, Michael Hu, Daniel R. Neuville, et al.. Structural, redox and isotopic behaviors of iron in geological silicate glasses: A NRIXS study of Lamb-Mössbauer factors and force constants. Geochimica et Cosmochimica Acta, 2022, 321, pp.184-205. ⟨10.1016/j.gca.2022.01.021⟩. ⟨hal-03857146⟩

HAL Id: hal-03857146

https://hal.science/hal-03857146v1

Submitted on 17 Nov 2022

HAL is a multi-disciplinary open access archive for the deposit and dissemination of scientific research documents, whether they are published or not. The documents may come from teaching and research institutions in France or abroad, or from public or private research centers.

L'archive ouverte pluridisciplinaire **HAL**, est destinée au dépôt et à la diffusion de documents scientifiques de niveau recherche, publiés ou non, émanant des établissements d'enseignement et de recherche français ou étrangers, des laboratoires publics ou privés.

HAL Authorization

Structural, redox and isotopic behaviors of iron in geological silicate glasses: a NRIXS study of Lamb-Mössbauer factors and force constants

Lamb-Mössbauer factors and force constants for Fe3+ and Fe2+ in silicate glasses from NRIXS and Mössbauer measurements

Mathieu Roskosz[1*], Nicolas Dauphas[2], Justin Hu[2], Michael Hu[3], Daniel R. Neuville[4], Dennis Brown[5], Wenli Bi[3], Nicole X. Nie[2,6], Jiyong Zhao[3], Esen E. Alp[3]

[1]Institut de Minéralogie, Physique des Matériaux et Cosmochimie, Muséum National d'Histoire Naturelle, Sorbonne Université, CNRS UMR 7590, Paris, 75005, France.

[2]Origins Laboratory, Department of the Geophysical Sciences and Enrico Fermi Institute, The University of Chicago, 5734 South Ellis Avenue, Chicago IL 60637, USA.

[3]Advanced Photon Source, Argonne National Laboratory, Argonne, IL 60439, USA

[4]Géomatériaux, Institut de Physique du Globe de Paris, CNRS, Paris University, Paris 75005, France

[5] Department of Physics, Northern Illinois University, DeKalb, IL 60115, USA.

[6]Earth and Planets Laboratory, Carnegie Institution for Science, Washington, DC 20015, USA

[*]Corresponding author

Abstract

We report a combined conventional Mössbauer and synchrotron Nuclear Resonant Inelastic X-ray Scattering (NRIXS) study of a series of glasses of geologically relevant compositions at temperatures ranging from 5 to 1223 K. We show that in materials of mixed Fe^{2+}-Fe^{3+} valences, the inverse of the Lamb-Mössbauer factor (also called recoil-free fraction) should correlate linearly with the fraction of the conventional Mössbauer peak that can be ascribed to Fe^{3+}. Extrapolating this linear relationship to pure Fe^{3+} and Fe^{2+} endmembers yields a ratio for the Lamb-Mössbauer factors *C* of Fe^{3+} and Fe^{2+} of ~1.21, independent, to the first order, of the bulk chemical composition of the glass. We show that the materials studied follow the harmonic approximation up to 1223 K for olivine and 773 K for basaltic glass, allowing us to extrapolate the value of C to different temperatures $C = (1.21 \pm 0.06)^{T/300}$. This calibration is used to correct previous acquired redox ratios, allowing us to estimate the mean force constants of the bonds involving Fe^{2+} and Fe^{3+} in geological glasses. We find a clear correlation between bond strength and iron redox ratio that is secondarily modulated by coordination effects in more alkali-rich felsic magmas. By examining synthetic model glasses, we find that the strength of Fe^{2+} bonds is influenced by the presence of network modifiers, more particularly K and Na. These observations explain the isotopic behavior of iron during magma differentiation. The refined ratio of Mössbauer factors for Fe^{2+} and Fe^{3+} is used to improve on calibrations of iron redox state in geological glasses using XANES spectroscopy.

1. Introduction

Iron is the most abundant multivalent element in igneous rocks. As such, it plays a unique role for both setting and recording redox conditions in the Earth. Its three valence states Fe^0, Fe^{2+}, and Fe^{3+} coexist within Earth but were partially separated during core formation and continental crust extraction. The oxidation state of iron in melts influences many of their properties, notably their rheology, thermal and electrical conductivities, and crystallization behaviors. Moreover, with appropriate thermodynamic calibration, the relative proportions of ferric (Fe^{3+}) and ferrous (Fe^{2+}) iron can be directly related to oxygen fugacity (fO_2) (Kennedy, G.C. 1948), a parameter that greatly influences the nature of volatiles degassed from magmas, thereby shaping the composition of Earth's atmosphere and its evolution through time (Kump et al., 2001; Gaillard et al., 2011; Andrault et al. 2017). Furthermore, the oxidation state of iron in mafic and ultramafic igneous rocks is a window into the redox conditions of the mantle (Christie et al., 1986; Canil et al., 1995; Bezos and Humler, 2005; Kelley and Cottrell, 2009; Cottrell and Kelley, 2011; Stolper and Bucholz, 2019, Le Losq et al., 2019). Determining the redox state of iron in natural magmas is therefore central to understanding the redox evolution of the Earth and its constituent reservoirs.

A variety of analytical techniques have been used to determine the iron redox ratio ($Fe^{3+}/\Sigma Fe$ with $\Sigma Fe = Fe^{2+}+Fe^{3+}$) in minerals and glasses including (but not restricted to) wet chemical determinations, Mössbauer spectroscopy and X-ray Absorption Near Edge Structure (XANES) spectroscopy (Neuville et al., 2021). The synchrotron technique of XANES has been increasingly used over the past decade because it has high spatial resolution, data collection is rapid, and the measurements are precise. Very early in the development of this method (e.g. Wilke et al., 2001; 2004, Farges et al., 2004; Giuli et al., 2002), it was found that the pre-edge centroid varies only between two endmember values for Fe^{2+} and Fe^{3+} and that the intensity varies with site-symmetry. Therefore, empirical calibration could in principle be unnecessary, as long as the site symmetries of Fe^{2+} and Fe^{3+} are known. This may be the case for canonical compositions such as “basaltic glasses” but more exotic natural or synthetic glasses would still require standardization against samples independently calibrated using wet-chemistry redox titration (Bezos and Humler, 2005) or Mössbauer spectroscopy (Berry et al., 2003; Wilke et al., 2005; Cottrell et al., 2009). Specifically, the calibration of XANES entails establishing an empirical relationship between (*i*) the normalized intensity and centroid

position of the pre-edge feature, and (*ii*) the coordination and redox state of iron. Such calibrations were done on a range of synthetic glasses with compositions that matched those encountered in natural settings (Berry et al., 2003; Wilke et al., 2005; Cottrell et al., 2009; Dauphas et al., 2014). In silicate glasses, Cottrell et al. (2009) and Dauphas et al. (2014) consistently found different calibration curves for rhyolitic compositions as compared to basalts, andesites and dacites, presumably reflecting differences in the coordination environment of iron in these glasses.

Conversion of Mössbauer data into iron redox ratio is also not straightforward. Zhang et al. (2015) pointed out that previously used data reduction procedures in Mössbauer spectroscopy had ignored the fact that the Lamb-Mössbauer factors (also called recoil-free fraction) of Fe^{2+} and Fe^{3+} in glasses differ significantly. The Lamb-Mössbauer factor (f_{LM}) is the probability that a photon with the correct energy will induce a nuclear transition in ^{57}Fe without energy loss due to recoil. Zhang *et al.* (2015) obtained a ratio $C = f_{LM}(\mathrm{Fe}^{3+})/f_{LM}(\mathrm{Fe}^{2+})$ of 1.256±0.153 for andesitic glass based on Mössbauer measurements done at various temperatures. The correction in $Fe^{3+}/\Sigma Fe$ ratios for values relevant to terrestrial settings range between ~15 and 25% relative, which is significant. Zhang et al. (2016) corrected Mössbauer data for this difference in Lamb-Mössbauer factors and provided a new set of XANES-Mössbauer calibrations. However, the value of C determined by Zhang et al. (2015) has large uncertainty and was only measured for an andesite glass. It is therefore unclear whether it can be applied to other compositions.

XANES and Mössbauer studies also have implications that extend beyond the calibration of spectroscopic approaches used in iron redox determinations. In particular, these techniques can provide clues on the valence state and coordination environment of iron in igneous minerals and melts, which affect iron equilibrium isotopic fractionation (Dauphas et al., 2014; Roskosz et al., 2015; Nie et al., 2020). Dauphas et al. (2014) acquired Nuclear Resonant Inelastic X-ray Scattering (NRIXS) data on the same glasses that they characterized by Mössbauer and XANES. They showed that the chemical bonds involving ferrous iron were characterized by much higher force constants in rhyolite than in less silicic glasses, affecting in turn iron isotopic fractionation during magma differentiation. The peculiar behavior of Fe in rhyolitic glass in XANES (Cottrell et al., 2009, Dauphas et al., 2014) was also found in NRIXS, suggesting that the coordination environment of iron in rhyolitic magmas must be different from that of basaltic, andesitic, or dacitic magmas. A question that remains to be addressed,

however, is whether the different force constants of iron bonds in rhyolite could be artifacts of an erroneous $Fe^{3+}/\Sigma Fe$ calibration if the value of C differed between rhyolite and other glasses.

We use here a multipronged approach to reassess how the composition of glasses affects iron bonding environment and iron redox determinations. New measurements and reevaluations of previously published data allow us to evaluate how iron isotopes could have been fractionated during mantle melting and magmatic differentiation. (*i*) We report new analyses by conventional Mössbauer spectroscopy at room and low temperatures of the samples previously described in Dauphas et al. (2014). (*ii*) We determine the ratio *C of the* recoil-free fractions of ferric and ferrous iron in glasses of basaltic, andesitic, dacitic, and rhyolitic compositions using Lamb-Mössbauer factors derived from NRIXS spectra. (*iii*) We study three simplified iron-bearing glasses with a silica content similar to rhyolites to understand how silicate melt structure affects the strength of iron bonds. (*iv*) We report NRIXS measurements of heated basaltic glass and olivine single crystals to evaluate the temperature dependence (or lack thereof) of iron bonds and recoil-free fractions.

Our results allow us to revise the calibration of redox determinations by Mössbauer and XANES taking into account the recoil-free fractions of Fe^{2+} and Fe^{3+} in four major groups of natural melts (basalts, andesites, dacites and rhyolites). This work also demonstrates that Fe-bonds in olivine and silicate glasses are sufficiently harmonic as to not affect Fe isotope partitioning over a temperature range of several hundreds of degrees. Finally, we show that the large amount of potassium and sodium present in rhyolitic melts leads to a significant increase of the iron force constant compared to basaltic and andesitic melts (at a given redox ratio). This can explain why granites and granitoids tend to have heavy Fe isotopic compositions.

2. Experimental and analytical protocols

2.1. Sample synthesis

The samples of basaltic, andesitic, dacitic and rhyolitic compositions were the same as those studied in Dauphas et al., (2014). Simplified potassium-, sodium- and magnesio-calcic ferrosilicate glasses were synthesized for the present study (labeled KS4, NS4 and CMS respectively). The compositions were selected as they allow us to evaluate how the coordination environment of iron is affected by the structure of the silicate melts (Mysen et al., 1980; 1985; Le Losq et al., 2020). The CMS series has a silica content intermediate between andesite and dacite, a NBO/T close to basalts and contains only Mg^{2+} and Ca^{2+} as network modifying cations, in proportions that allow these glasses to easily melt and quench (relatively high CaO/MgO ratio). The NS4 and KS4 series have silica contents close to rhyolites (slightly lower though in order to avoid risks of unmixing during the synthesis Richet et al., 2006) and only contain either K^+ or Na^+ in order to isolate their effects on the coordination chemistry and valence state of iron. Sodic and potassic binary silicate glasses are known to be hygroscopic. A special care was therefore paid to store them in dry conditions. Furthermore, sample surfaces were gently polished before each analytical session. Finally, NRIXS spectra of the reduced KS4 were collected twice on the same sample during two different sessions separated by several months. No changes could be observed indicating that these iron rich potassic glasses did not suffer significant hydration during the course of this study.

All samples analyzed (including KS4, NS4 and CMS) in this study were enriched in ^{57}Fe to reduce acquisition time. Glasses were all prepared from mixtures of reagent grade SiO_2, Al_2O_3, $CaCO_3$, MgO, Na_2CO_3, K_2CO_3, TiO_2, and Fe_2O_3 that were first fired at 300 to 1000 °C. The starting material was melted in air at 1550°C for 1h in a thin-walled Pt crucible and was then finely crushed. Glasses were then remelted for 1h and quenched on a Cu plate.

Final syntheses were performed in vertical gas-mixing furnaces (Gero, CRPG, Nancy, France) using the wire-loop method for natural analogs and CMS glasses. The oxygen fugacity (fO_2) was controlled using CO/CO_2 gas mixtures as detailed in Dauphas et al. (2014). Three nominal oxygen fugacities were applied to the samples at 1550 °C: $Log(fO_2)=-0.7$ (air), $Log(fO_2)=-2.4$ (QFM+2.5), $Log(fO_2)=-8$ (IW+0.3). Limited volatilization was observed during these syntheses as shown in Table 1.

The KS4 and NS4 reduced glasses were prepared in a piston cylinder apparatus (LMV, Clermont-Ferrand, France). The reduction was performed in graphite capsules using a non-

end loaded piston cylinder in order to avoid large evaporative loss of potassium and sodium. For those samples, about 80 mg of the glass samples prepared in air were packed in a graphite capsule (4mm OD) and placed in a salt/pyrex/MgO assembly. Synthesis was done at 1300°C and 1 GPa for 1h. Strictly speaking, these samples were equilibrated at an unknown fO_2 below the graphite-CO buffer. For simplicity, we labelled them `IW` just as the most reduced glasses prepared for each other series.

The chemical compositions of glasses were determined after synthesis with an electron microprobe (Cameca SX100 at the UMET laboratory; University of Lille) operating at 15kV and 15nA beam current. Albite, MgO, Fe_2O_3, orthoclase, wollastonite, $MnTiO_3$ standards were typically used to calibrate the microprobe. Analyzed glass compositions (Wt%) are summarized in Table 1.

In addition to these glass samples, olivine single crystals, enriched in ^{57}Fe were synthesized to evaluate whether the strength of iron bonds is affected by temperature. The protocol described in Sio et al. (2018) designed to study iron isotopic diffusion in oriented olivine single-crystal was adapted here. San Carlos olivine single crystals ($Fo_{88.8}$) were optically selected and cut into roughly oriented parallelepipeds. They were placed in an alumina crucible filled by a mixture of oxides (66 wt% ^{57}FeO – 34 wt% MgO) that sintered around the crystals upon heating. This configuration buffered the experiment at low silica activities (a_{SiO2}), which in turns likely affected the Mg-Fe exchange rate through the crystal/oxide interface. Experiments were run at ambient pressure in a Gero furnace at CRPG (Nancy France). A CO-CO_2 gas mixture was used to control the oxygen fugacity (f_{O2}), which was set to 1.5 log units below the quartz-fayalite-magnetite (QFM; 72.75% CO2+27.25% CO gas mixture) buffer at 1400 °C. The crucible was initially placed in a vertical oven at 1000°C and a gas flow of 300 cm^3/min to flush the air trapped into the oxide powder for 10 hours. Upon heating, the target temperature of 1400°C was reached in 15 minutes and the flow was decreased to 100 cm^3/min. Samples were then isothermally annealed for 290 hours. At the end of the experiment, samples were rapidly removed from the hot spot of the furnace and quenched before exposure to air. Recovered samples consisted of single crystals embedded in a loosely sintered black powder. This crust was easily removed after a gentle grinding using silicon carbon abrasives. Crystals were then cut into ~ 150 µm slices with the help of a wire saw. Samples were deposited on a SEM sample holder and inspected by Scanning Electron Microsopy to check that the oxide crust was completely removed (Fig. 1a).

211

212 *2.2. Room temperature NRIXS spectroscopy*

213 Details on the synchrotron technique of NRIXS are available in Chumakov and Sturhahn
214 (1999); Sturhahn et al. (1995); and Seto et al. (1995). The measurements were performed at
215 beamline 3-ID-B of the Advanced Photon Source (APS) at Argonne National Laboratory. The
216 storage ring was operated in top-up mode with 24 bunches separated by 153 ns. Two
217 Avalanche Photon Diode (APD) detectors positioned at 180° from each other and
218 perpendicular to the incident X-ray beam direction were used. The sample was positioned in
219 between those two detectors. The average energy resolution (full width at half maximum -
220 FWHM) was 1.33 meV. The monochromator was tuned from ~ -130 meV to ~+130 meV with
221 a step size of 0.25 meV and a collection time of 2-3 s per step. The number of scans collected
222 per sample depended on its ^{57}Fe content and ranged from 2 to 12 scans. The direction of the
223 scans was alternated from low to high energy and vice versa to mitigate the effect of any drift
224 in the instrument response with time.

225 The signal measured is proportional to the phonon excitation probability density
226 function *S(E)*. After elastic peak removal and some normalization, this function can be used to
227 calculate the iron phonon density of states (PDOS) (Sturhahn et al., 1995). The density of
228 states is the energy distribution of network vibration modes. Through statistical mechanics,
229 this distribution relates to the thermodynamics of the sample. A large array of physical
230 properties relevant to the field of mineral physics can be derived from these spectra. Among
231 them, this study particularly focuses on the mean force constant of the bond holding iron in
232 position $\langle F \rangle$, the coefficients in the polynomial expansion of iron reduced partition function
233 ratios used in isotopic geochemistry (β-factors), and the Lamb-Mössbauer factor (f_{LM}).
234 Dauphas et al. (2012) and Hu et al. (2013) showed that the iron reduced partition function
235 ratios used to calculate equilibrium isotopic fractionation between phases could be calculated
236 directly from *S(E)*. At the high temperatures relevant to igneous and metamorphic
237 geochemistry, the fractionation between ^{56}Fe and ^{54}Fe takes the form,

238 $$1000 \ln \beta_{56Fe/54Fe} \simeq 2904 \frac{\langle F \rangle}{T^2}, \qquad (1)$$

239 where *T* is in Kelvin. $\langle F \rangle$ is in N/m and is proportional to the 3rd centered moment of *S(E)*,

240 $$\langle F \rangle = \frac{M}{E_R \hbar^2} \int_{-\infty}^{+\infty} (E - E_R)^3 \, S(E) dE, \qquad (2)$$

241 with M the mass of ^{57}Fe, $\hbar$ is the reduced Planck constant, and E_R is the free recoil energy.

When the force constant is higher than 100 N/m, which is the case for Fe-bearing oxides and silicates, equation (1) gives an approximation of the true β-factors with an accuracy of better than 99% down to 300 °C. At lower temperature, a more general equation gives the β-factors through a polynomial expansion in inverse even powers of the temperature,

$$1000 \ln \beta_{^{56}Fe/^{54}Fe} \simeq \frac{A_1}{T^2} + \frac{A_2}{T^4} + \frac{A_3}{T^6}, \qquad (3)$$

where the coefficients A_1, A_2, and A_3 can be calculated from the moments of *S(E)* (Eq. 3 of Dauphas et al., 2012; $A_1 = 2904\langle F \rangle$). The Lamb-Mössbauer factor is the ratio of recoil-free to total nuclear resonant absorption or the probability that a photon with the correct energy will induce a nuclear transition in ^{57}Fe without energy loss due to recoil. It is calculated during normalization of the phonon excitation probability density function *S(E),* and it can also be calculated from the inverse moment of the PDOS *g(E)* (Sturhahn et al., 1995; Hu et al., 2013; Dauphas et al., 2018).

Data reduction was done with a Mathematica software (SciPhon 1.1.0) described in Dauphas et al. (2018). Its main features are that it calculates all the parameters needed for iron isotope geochemistry, and it propagates all sources of errors (*i.e.*, counting statistics, baseline subtraction, energy scaling) on the derived parameters.

2.3. High temperature NRIXS spectroscopy

Heating experiments are time consuming and difficult to implement, so we focused on just two compositions. The first one is a basalt glass synthesized in air containing 57% Fe^{3+} and 43 % Fe^{2+} (Dauphas et al., 2014). This mixed valence sample allows us to evaluate whether iron in either oxidation state presents some anharmonic behavior. As discussed below, we did not detect any change in the force constant of iron with temperature, so we did not examine other glass compositions. We also studied olivine single crystals containing pure ^{57}Fe as Fe^{2+} prepared as described above.

The samples were heated using a wire-heating furnace (Neuville et al., 2014 and references therein) modified from the design of Mysen and Frantz (1992). The wire-heating system consists of a power supply and Pt wire with a tiny hole pierced in its center. The wire is heated through Joules effect by increasing the electrical current running through it. The relationship between the electrical current and the temperature is calibrated by melting single

component phases of known melting temperatures such as $NaNO_3$ (613 K) and $CaSiO_3$ (1813 K) (see Neuville and Mysen 1996 for more details). This calibration is done prior to the beamtime session and melting of the single component phases is optically assessed. Because the calibration can be affected by gases in the surrounding atmosphere, the temperature is also measured with a pyrometer during the experiment.

All experiments were done under subsolidus conditions in air. Two APD Detectors were used to collect the NRIXS signal (Fig. 1b). The basaltic glass was measured at three temperatures of 300, 558, and 773 K. Olivine was also measured at three temperatures of 300, 773, and 1223 K. Before and after measurements, synchrotron Mössbauer spectra were collected at the same beamline to monitor any significant redox or structural evolution. No changes were observed. There were several limitations to the temperature that we could reach. First, force constants can only be measured in solids, so all measurements were subsolidus. For the glass, we stayed below the glass transition temperature to also avoid crystallization. This strict limitation is due to the fact that the signal intensity is proportional to the *Lamb-Mössbauer factor* of the sample. This factor drops down to 0 at the solid-liquid transition as the fraction of recoil-free iron vanishes. This intensity collapse was used to study melting points of compressed iron and to study local dynamics of Fe species in silicate glasses and melts close to the glass transition temperature (Jackson et al., 2013; Weigel et al., 2010) Second, the Lamb-Mössbauer factor severely decreases when the temperature increases and the multiphonon contribution increases, which makes it difficult to extract useful data from the phonon excitation probability density function (see the result section). For olivine, no useful data could be acquired above 1223 K.

2.4. Conventional and low-temperature Mössbauer spectroscopy

In order to better characterize reduced samples for which the determination of the redox ratio by conventional Mössbauer spectroscopy is not trivial ($Fe^{3+}/\Sigma Fe<10\%$), the 4 most reduced glasses analyzed in Dauphas et al. (2014) were measured a second time at low temperature (5 and 90 K in the case of the basalt). The basalt prepared in air was also analyzed at 90 K. The three new series of glasses KS4, NS4 and CMS were analyzed at room temperature (Fig. 2). The Mossbauer Spectroscopy measurements were performed in transmission mode using a

constant acceleration spectrometer. A fill type liquid Helium cryostat was used for low temperature measurements. The point source was ^{57}Co/Pd about 5 mCi. High purity Germanium detector was used for recording the transmitted photons. Data was analyzed using WinNormos commercial program package provided by WissEl Co. The primary purpose of the Mossbauer spectra was to find Fe2+/Fe3+ ratio, and temperature dependence of hyperfine parameters. The line widths used to fit the spectra were wide enough to get a good fit, without invoking gaussian distribution of quadrupole of isomer shift values. Nonetheless, since all spectra were collected in the similar conditions and fits to the data performed in a consistent way, we compare the IS and QS parameters derived from this procedure in the discussion, focusing on the systematic variations observed.

3. Results

3.1. Reassessment of redox ratios based on conventional Mössbauer spectra with a special emphasis on reduced glasses

Processing of the data was performed using two to four symmetric lines. In each case, the minimum number of lines required to adjust the fit to the data was preferred. Derived Mössbauer parameters are listed in Table 2. No magnetic ordering (not even a weak long range magnetic correlation) was observed in our spectra down to 5 K**.** The assignment of some lines is not trivial because they exhibit IS and QS values deviating from the typical ranges covered by ferric and ferrous iron in glasses (Dyar et al., 2006). Similar observations were recently made by Berry et al. (2018). The IS and QS values determined here are comparable to values derived by Berry et al. (2018). In particular, a minor component found in all 'IW' samples with relatively low IS and QS for typical Fe^{2+} (IS close to 1 mm/s, QS close to 1.3 mm/s) was also observed by Solomatova et al. (2017) on the same glasses and by Berry et al. (2018). Such signatures were also found earlier by Rossano et al. (1999) on very reduced tektites and attributed to Fe^{2+}. We therefore conclude that all the glasses labeled 'IW' (the most reduced samples of each series) do not contain measurable amount of Fe^{3+} (i.e. less than 2%).

Turning to simple glasses KS4, NS4 and CMS, we note that at constant oxygen fugacity during melting in air at the same temperature, iron in potassic glasses and in sodium-bearing glasses, is more oxidized than in the CMS glass. This was documented previously in synthetic and natural glasses (*e.g.* Kress and Carmichael, 1988, 1991; Lange and Carmichael, 1989; Moretti, 2005; Borisov et al., 2017). Again, for the samples KS4, NS4 and CMS prepared in reducing conditions of ~IW, no measurable amount of ferric iron could be detected in the Mössbauer spectra.

3.2. NRIXS spectra of simple glasses and derived physical properties

The projected partial densities of states (DOS) collected on simplified glasses are presented in Figure 3 (a, b). A direct comparison with spectra acquired earlier on synthetic natural glasses is also displayed in Figure 3 (c-f). All the physical properties calculated from these data are also tabulated (Table 3). The iron PDOS show significant variations among these glasses at a given oxygen fugacity (Fig. 3 a, b). We first note that the main peak is thinner for reduced than for oxidized glasses. The finest peak is observed for CMS IW, the PDOS of which

only displays a broad and weak tail at energy higher than 50 meV. Sample NS4 IW shows a more intense peak at ~65 meV. Such a peak (slightly more intense) is also observed for KS4 IW at a slightly lower energy. Turning to oxidized glasses, the main peak at low energy is overall broader for NS4 and KS4 than for CMS. This may essentially be due to the fact that in air, these glasses are overall more oxidized than CMS. Furthermore, a broad peak centered at 70 meV (not present in reduced glasses) is observed for all these samples. It is more prominent in KS4 and NS4 than in CMS. This may again be due to the more oxidized nature of these glasses as compared to CMS. This broad peak exhibits a nicely defined shoulder at even larger energy (85 meV) in CMS and NS4 glasses. The KS4 glass does not reveal such a clear shoulder but instead, a broad, intense continuous decay of the signal (Fig. 3a). These peaks (not present in PDOS of reduced glasses) could tentatively be assigned to a ferric iron contribution and to the coordination of sites occupied by iron atoms in the network, as discussed below. Turning to the comparison with natural compositions, the most salient observation is that CMS and tholeiitic basalts have strikingly similar PDOS both for reduced and oxidized glasses (Fig. 3 c, d). Even the subtle variations such as the small peak at 85 meV are found in both simplified and natural glasses. The same similarities are obvious between NS4, KS4 and rhyolites (Fig. 3 e,f). This has strong implications in terms of structural role of iron as seen by NRIXS as discussed below. For instance, aluminum has no influence on the iron coordination chemistry since simplified glasses do not contain any aluminum.

3.3. Spectroscopic determination of the Lamb-Mössbauer factors

Zhang et al. (2015, 2016) made the case that the recoil-free fractions differ for Fe^{2+} and Fe^{3+}. The Lamb-Mössbauer factor can be precisely quantified using NRIXS data. It can either be calculated from the phonon excitation probability density function *S(E)* or the partial PDOS *g(E)* (Dauphas et al., 2018 and references therein). Table 4 summarizes all the f_{LM} extracted from the samples studied here together with the values derived for previous measurements of basaltic, andesitic, dacitic, and rhyolitic glasses by Dauphas et al. (2014). This factor varies from a glass to the other and seems to exhibit some weak compositional dependences with optical basicity, silica content, redox state (See Supplementary Online Material). These correlations are clearly multivariate and may also correlate with bulk properties such as Debye sound velocity and compressibility because all these properties are dominated by the position

and intensity of the first main peak of PDOS. A multivariate ACP analysis could eventually shade some interesting lights on these entangled correlations but this would need a much larger database.

As the most reduced samples of each series only contain Fe^{2+}, the recoil-free fraction for ferrous iron is directly determined. This is not true for ferric iron because even the most oxidized samples of each series contain significant amounts of ferrous iron. To estimate f_{LM} for Fe^{3+}, one can examine how f_{LM} correlates with $Fe^{3+}/\Sigma Fe$ on a range of glasses synthesized under different oxygen fugacities, and then extrapolate the correlation to a $Fe^{3+}/\Sigma Fe$ of 1. The difficulty with this approach is that the $Fe^{3+}/\Sigma Fe$ estimated by Mössbauer depends on the ratio *C* of the Lamb-Mössbauer factors of Fe^{3+} and Fe^{2+}, noted f_3 and f_2 respectively ($C=f_3/f_2$). For each glass composition series (basalt, andesite, dacite and rhyolite) f_{LM} was plotted against '*raw*' redox ratios determined by conventional Mössbauer spectroscopy at 300 K as the ratios of the areas of the spectral lines for ferric and ferrous iron. For all series of glasses, a linear correlation was observed between the apparent redox ratios and f_{LM}. We therefore assumed in the following that, at the first order, f_{LM} of intermediate glasses containing both ferric and ferrous irons could be described as a linear mixture of two endmembers for ferric and ferrous iron (again noted f_3 and f_2 respectively).

We therefore assume that the f_{LM} value of a given glass is given by a linear combination of the end-members f_2 and f_3,

$$f_{LM} = x_3 f_3 + (1 - x_3) f_2, \quad (4)$$

where $x_3 = Fe^{3+}/\Sigma Fe$ is the fraction of Fe^{3+} in total iron. The absorption areas of Mössbauer lines produced by Fe^{3+} and Fe^{2+} (S_3 and S_2 respectively) are related to the abundances of the ions (N_{Fe3+} and N_{Fe2+}) and to the recoil-free fractions of each ion at a given temperature, according to,

$$S_3/S_2 = C\frac{N(Fe^{3+})}{N(Fe^{2+})} = C\frac{x_3}{1-x_3}. \quad (5)$$

where $C=f_3/f_2$. If we note $\mathcal{s} = S_3/(S_3 + S_2)$ the ratio of the surface areas of the peaks of Fe^{3+} relative to the total area of the Mössbauer spectrum, we can combine Eqs. 4 and 5 to establish the following relationships,

$$\frac{1}{f_{LM}} = \frac{1-\mathcal{s}}{f_2} + \frac{\mathcal{s}}{f_3}, \quad (6)$$

$$\frac{1}{f_{LM}} = \frac{1}{f_2} + \frac{1}{f_2}\left(\frac{1}{C} - 1\right)\mathcal{s}. \quad (7)$$

These equations show that if we plot $1/f_{LM}$ measured by NRIXS against $\mathcal{S}$ measured by conventional Mössbauer, the points should define a straight line of slope $1/f_3 - 1/f_2 = 1/f_2\,(1/C - 1)$ and of intercepts $1/f_2$ at $\mathcal{S} = 0$ and $1/f_3$ at $\mathcal{S} = 1$. In Fig. 4, $1/f_{LM}$ is presented against $\mathcal{S}$ for all synthetic glass samples. The slope and intercept of the best-fit lines were calculated and then f_2, f_3, and C were derived. Uncertainties on these values were estimated by bootstraping the residuals from the best-fit line. For each glass composition, the results are compiled in Table 4.

Zhang et al. (2015) obtained a C value of 1.256±0.153 for andesite. Our estimate for approximately the same composition is 1.171±0.026, which is in good agreement with the value that they propose but of much higher precision. Furthermore, our data suggest that a single value of C (1.21±0.06) could be used to correct Mössbauer data collected at room temperature (~300K) on the entire range of glasses studied here (from simple ternary glasses such as NS4 and KS4 to analogues of natural glasses). With this correction in hand, we reappraise below the XANES *vs*. Mössbauer and the <F> *vs*. redox calibrations.

3.4. High-T NRIXS spectra and physical properties of basalt glass and olivine

The NRIXS spectra for basaltic glass synthesized in air and olivine were acquired over a range of temperatures. The PDOS are plotted in Fig. 5 and the derived parameters are compiled in Table 5. For olivine at 1223 K, the Lamb-Mössbauer factor derived from the data is ~0.23. This means that S(E) contains a large multiphonon contribution and under these circumstances, we were unable to calculate a reliable PDOS. We were also unable to calculate many of the parameters that derive from both *g(E)* and *S(E)*, including the force constant of iron bonds. We only report in Table 5 the data that are deemed to be reliable.

The PDOS of basaltic glass containing 57% Fe^{3+} and 43% Fe^{2+} does not change when the temperature increases from room temperature (300K) to 773 K. Expectedly, the Lamb-Mössbauer factor decreases from 0.685 to 0.375. The thermal agitation associated with this temperature increase is associated with increases in the mean square displacement from 0.0071 to 0.0184 $Å^2$, internal energy/atom from 29.9 to 68.3 meV, kinetic energy/atom from 15.0 to 34.1 meV. The mean force constant on the other hand does not change significantly, staying at ~290 N/m at all temperatures. This constancy of the force constant is expected for a harmonic system. For basaltic glass in air, Dauphas et al. (2014) had previously reported

444 values of 0.668, 0.0076 Å^2, 30.1 meV, 15.0 meV, and 292 N/m, for the Lamb-Mössbauer factor,
445 mean square displacement, internal energy, kinetic energy, and force constant, respectively,
446 which are all in excellent agreement with the value reported here (Table 5).
447 The three olivine measurements at 300, 300, and 773K yield variable PDOS. We believe
448 that these differences are not due to temperature but rather to crystal orientation of the
449 olivine single crystals that were measured as the largest difference is between the two PDOS
450 acquired at 300K (Fig. 5). We indeed find that the two olivine PDOS at 300K, although very
451 different in their shapes, yield similar values for the Lamb-Mössbauer factor (0.757 *vs*. 0.769),
452 mean-square displacement (0.00523 *vs*. 0.00493 Å^2), internal energy (28.67 *vs*. 29.15 meV),
453 kinetic energy (14.33 *vs*. 14.57 meV), and force constant (202 *vs*. 245 N/m). These values are
454 also very similar to our previous room temperature NRIXS measurement of olivine (0.766,
455 0.00499 Å^2, 28.87 meV, 14.43 meV, 197 N/m for the same parameters; Dauphas et al., 2014).
456
457

4. Discussion

4.1. Harmonic or anharmonic behavior of iron in basaltic glass and olivine

To apply the results from NRIXS experiments performed at room temperature to geological settings, the assumption is often made that the bonds are harmonic, meaning that the interatomic potential varies with the square of atomic displacement. Under this assumption, the force constant of iron bonds measured at room temperature can be used directly to calculate equilibrium isotopic fractionation between coexisting phases at any temperature (Dauphas et al., 2012). Anharmonicity must however be present at some level as it is one of the main mechanism responsible for thermal expansion. For example, the volume of forsterite expands by 8% when the temperature is increased from 300 to 2300 K (Bouhifd et al., 1996) and no expansion would be present if the bonds were perfectly harmonic. If the bonds are perfectly harmonic, then the force constant of those bonds should not vary with temperature. Conversely, anharmonicity in interatomic potentials would be manifested as an apparent variation of the force constant of the iron bonds as temperature changes and the potential is explored over a range of interatomic distances. For example, Hu et al. (2013) considered an anharmonic potential V including a quartic term,

$$\frac{\partial^2 V}{\partial z^2} = K + Az + \frac{B}{2}z^2, \quad (8)$$

where z is the atomic displacement, K is the spring constant, and B is the anharmonic term. They showed that for such a potential, the apparent mean force constant $\langle F \rangle$ given by the third moment of the NRIXS measurements will be,

$$\langle F \rangle = K + \frac{B}{2}\langle z^2 \rangle, \quad (9)$$

where $\langle z^2 \rangle$ is the atomic mean square displacement, which can be derived from NRIXS spectra using the equation $\langle z^2 \rangle = -\ln(f_{LM})/k^2$ with k the angular wavenumber (see Dauphas et al., 2017 and references therein for details). In Fig. 6, the apparent force constant $\langle F \rangle$ is presented against $\langle z^2 \rangle$ for basalt glass and olivine crystals measured at different temperatures. No measurable variation in the force constant of Fe can be resolved even when the mean square displacement increases by a factor of ~2.6. For the force constant, temperatures up to 773 K (500 °C) were investigated. The mean square displacement increases more or less linearly with temperature, which imply that although the temperature investigated do not reach those

encountered in igneous systems, they are sufficient to rule out the presence of large anharmonic effects for the force constant. It is therefore reasonable to use iron force constants measured at room temperature to calculate equilibrium isotopic fractionation between melts and minerals at temperature relevant to igneous systems. Further work is nevertheless needed to ascertain whether harmonicity holds up to the temperature of silicate melts where there is the most chance to detect anharmonic behavior. Because the Lamb-Mössbauer factor decreases with increasing temperature, it is not possible to test for anharmonicity beyond the temperatures investigated here and another approach such as first-principle calculations (Pinilla et al., 2021) should be used.

The temperature dependence of the Lamb-Mössbauer factor was also studied. Under the harmonic approximation, the Lamb-Mössbauer factor is expected to change with temperature following (Dauphas et al. 2018 and references therein),

$$ln\, f_{LM} = -\frac{k^2\hbar^2}{M}\int_0^{+\infty}\frac{1}{2E}coth\left(\frac{E}{2k_BT}\right)g(E)dE, \quad (10)$$

with $\hbar$ the reduced Plank constant and M the mass of the nuclear resonant isotope. For x approaching 0, $coth(x)\sim 1/x$ so at high temperature the above equation is extrapolated as:

$$ln\, f_{LM} \simeq -k^2\frac{d\langle z^2\rangle}{dT}T \quad (11)$$

To first order, f_{LM} should exponentially approach zero as the temperature increases. To test this behavior, the values measured at high temperature are compared with the predicted evolution using Eq. 10 and taking the lowest temperature PDOS, $g(E)$ to calculate the value in the integral (Fig. 7). The decrease of the Lamb-Mössbauer factor f_{LM} is found to be well accounted for by the harmonic approximation.

The temperature dependence of C was also investigated within the harmonic approximation. The PDOS of Dauphas et al. (2014) were used to calculate how the f_{LM} values of the basalt, andesite, dacite, and rhyolite glasses synthesized with different $Fe^{3+}/\Sigma Fe$ ratios should change with temperature based on their room temperature PDOS measurements. At each temperature, the values of C were calculated by extrapolating the computed f values to $Fe^{3+}/\Sigma Fe$ ratios of 0 and 1. As shown, C starts from $C = 1$ at $T = 0$, and increases with T (Fig. 7). A simple parametric formula is proposed to account for this dependence. For that purpose, a Debye PDOS with a cutoff energy E_D was considered

$$g(E) = 3E^2/{E_D}^3; E \le E_D, \quad (12)$$

$$g(E) = 0; E > E_D. \quad (13)$$

With this assumption, the Lamb-Mössbauer factor f_{LM} can be written according as,

$$\ln f_{LM} = -\frac{k^2\hbar^2}{M}\int_0^{E_D} \coth\left(\frac{E}{2k_BT}\right)\frac{3E}{2{E_D}^3}\mathrm{d}E. \quad (14)$$

At high temperature, Eq. 14 can be approximated using Taylor expansion (This approximation was tested numerically and found to be valid above 150 K) and thus,

$$\ln f_{LM} \simeq -\frac{k^2\hbar^2}{M}\int_0^{E_D}\left(\frac{2k_BT}{E}+\frac{E}{6k_BT}\right)\frac{3E}{2{E_D}^3}\mathrm{d}E, \quad (15)$$

which can be further simplified to:

$$\ln f_{LM} \simeq -\frac{k^2\hbar^2}{M}\left(\frac{3k_BT}{{E_D}^2}+\frac{1}{12k_BT}\right). \quad (16)$$

If we now consider that Fe^{2+} and Fe^{3+} have Debye cutoff energies of $E_{D,Fe^{2+}}$ and $E_{D,Fe^{3+}}$, it follows from Eq. 16 that:

$$\ln C = \ln\frac{f_{LM,Fe^{3+}}}{f_{LM,Fe^{2+}}} \simeq -\frac{k^2\hbar^2}{M}\left(\frac{1}{{E_{D,Fe^{3+}}}^2}-\frac{1}{{E_{D,Fe^{2+}}}^2}\right)3k_BT, \quad (17)$$

The value of C can then be parameterized as (with θ a constant),

$$C = e^{\theta T}, \quad (18)$$

with θ a constant. The Debye model predicts a linear relationship between $\ln C$ and T, which is verified in figure 7 (a near linear relationship that goes through the origin is observed). For geological glasses, $C = (1.21 \pm 0.06)^{T/300}$, where the uncertainty is given as 1σ.

4.2. Determination of 'true' redox ratios and reassessment of a distinct XANES-Mössbauer calibration for rhyolitic glasses

The accuracy of the determination of redox ratios from Mössbauer spectra depends on several assumptions and parameters. An important parameter is the ratio of the recoil-free fractions of Fe^{3+} and Fe^{2+} ions (f_3 and f_2 respectively), which represent the fractions of 14.4 keV X-rays interacting resonantly with the ^{57}Fe ions through a nuclear transition. The absorption areas of Mössbauer lines produced by Fe^{3+} and Fe^{2+} (S_3 and S_2 respectively) are indeed related to the abundances of the ions (N_{Fe3+} and N_{Fe2+}) and to the recoil-free fractions of each ion at a given temperature, according to Eq.5, where $C=f_3/f_2$, the recoil-free fraction, related to the mean-square atomic displacement. As mentioned above, the standard assumption is to consider that C=1 (e.g. Mysen and Virgo, 1985; Dyar et al., 1987; Jayasuriya et al., 2004; O'Neill et al., 2006; Rossano et al., 2008; Cottrell et al., 2009; Borisov and

McCammon, 2010; Berry et al., 2018). This simplification is in part justified because some comparisons between uncorrected room-temperature Mössbauer measurements and redox ratios determined by other methods have found good agreement with wet chemical determinations (Mysen and Virgo, 1985; ~~Dingwell, 1991;~~ Magnien et al., 2004, Wilke et al., 2005). However, some discrepancies have also been found (e.g. Righter et al., 2013).

As recoilless interactions depend on bond strengths and are affected by network vibrations, the values of f_i have no reason to be the same for Fe^{3+} and Fe^{2+} in minerals and glasses. The recoil-free fraction has been determined experimentally from a determination of the Debye temperature derived from the change of the isomer shift (IS) with temperature (Niemantsverdriet et al., 1984b; De Grave et al., 1985; Dyar et al., 2012). Chen and Yang (2007) and Zhang et al. (2015) used another method based on the temperature-dependence of the ratios of Fe^{3+} and Fe^{2+} Mössbauer lines. All these approaches are indirect and time-consuming. For this reason, available data for *C* for glasses of geological interest is very limited. Studies of silicate minerals have found values of *C* at room temperature ranging from ~1.0 in biotite (Bancroft and Brown, 1975) to 1.4 in garnet (Woodland and Ross, 1994; Dyar et al., 2012), but typical values are closer to 1.2 (De Grave and Van Alboom, 1991). To our knowledge, the only study on glasses focused on two andesitic glasses (Zhang et al., 2015). They found values of 1.151 ± 0.118 and 1.256 ± 0.0153 for the two samples that they analyzed. Zhang et al. (2016) also proposed a *C*-value of 1.124 for rhyolite glass, from a comparison between room temperature Mössbauer and wet chemistry data from Cottrell et al. (2009).

Our experimental data significantly expand this database for glasses to encompass basalt, andesite, dacite and rhyolite. Indeed, the Lamb-Mössbauer factor is a direct output of the processing of NRIXS data (Table 3; Dauphas et al., 2014). We therefore used newly acquired NRIXS spectra (KS4, NS4 and CMS) and previously published data (Dauphas et al., 2014) to derive experimental values of *C* for a complete array of geologically relevant glass compositions (Table 4). As presented before compositional effects are very limited. Within analytical uncertainties a single value of *C* (1.21±0.06) captures the behavior of iron in tholeiitic basalts, andesites, dacites and rhyolites (Table 4). This value encompasses the previously estimated values for andesite from Zhang et al. (2015; 2016). Our result therefore confirms the conclusion of Zhang et al (2015) that conventional Mössbauer without correction for the difference in Lamb-Mössbauer factors of ferrous and ferric iron overestimates $Fe^{3+}/\Sigma Fe$ of glasses. We further demonstrate that the correction that needs to be applied is not

583 dependent on the glass composition to the first order.

584 The $Fe^{3+}/\Sigma Fe$ reported by Dauphas et al. (2014), as well as most literature data, were
585 not corrected for the difference in Lamb-Mössbauer factors between Fe^{2+} and Fe^{3+} and are
586 therefore presumably offset by up to 20% relative to the true values. We have therefore re-
587 evaluated those data by applying a correction using our new estimates of *C*. The corrected
588 $Fe^{3+}/\Sigma Fe$ and force constants of the Fe^{2+} and Fe^{3+} endmembers are compiled in Table 4.

589 Our results also confirm that there is a significant difference in the XANES *vs*.
590 Mössbauer calibration between rhyolite on one hand and basaltic compositions on the other
591 hand (Cottrell et al., 2009; Dauphas et al., 2014). In order to illustrate this difference, we have
592 compiled available data from the literature. As conditions of XANES data collection vary from
593 one study to another, the energy of the centroid of the pre-edge feature cannot be compared
594 directly. Strictly speaking, the background treatment induces the largest error in the whole
595 data processing and makes the transfer of centroid values from one study to another almost
596 impossible, unless it can be checked on model compounds. However, as a first order
597 approximation, assuming an inter-laboratory consistent redox determination by Mössbauer
598 spectroscopy or wet chemistry, we have rescaled all available data (see figure captions for
599 more details). Our compilation demonstrates that most natural glasses define a single trend
600 in centroid energy vs. redox state, with the notable exception of rhyolites that define a
601 separate line (Fig. 8). Zhang et al. (2016) proposed that this feature, noted by Cottrell et al.
602 (2009) and Dauphas et al. (2014), may at least in part be caused by different *C*-values for
603 basalts, andesites and rhyolites. Our results invalidate this hypothesis. Instead, they sustain
604 our initial claim (Dauphas et al., 2014) that redox state of rhyolitic glasses cannot be quantified
605 from XANES spectra using the basalt glass calibration. Fiege et al. (2017) proposed that a single
606 curve could account for both mafic and felsic glasses. We note that their calibration does not
607 include data for highly reduced rhyolitic compositions that exhibit the largest discrepancy
608 relative to the "basaltic" calibration line (Fig. 8). Therefore, this calibration is only valid when
609 $Fe^{3+}/\Sigma Fe > 0.3$ as pointed out by Fiege et al. (2017), where the compositional dependence is
610 smaller. Their calibration curve is quite uncertain (the envelope of the 95% confidence interval
611 for the prediction is large), which stems in part from the assumption that composition has no
612 significant effect on the calibration. Here, we have included their data in Figure 8. Their data
613 for rhyolite are in excellent agreement with ours (and those of Cottrell et al., 2009). It is of
614 note that their data for andesites and dacites also plot on the same "rhyolitic" calibration line

(black dotes following the blue curve on Figure 8). This is at odd with our dataset where andesites and dacites plotted on the "basaltic" line. There are therefore some ambiguities concerning these intermediate compositions that may need further investigation. Still, based on the two parametric equations describing the fit to the data (Fig. 8), we propose that a robust calibration of XANES to derive redox ratios of rhyolitic glasses (and possibly andesitic and dacitic ones) is achieved by applying an offset to the basalt regression curve of the form

$$\Delta E = 0.37 \cdot (\mathrm{Fe^{3+}}/\Sigma\mathrm{Fe})^2 - 0.78 \cdot (\mathrm{Fe^{3+}}/\Sigma\mathrm{Fe}) + 0.39\,, \qquad (19)$$

where ΔE is the centroid energy difference in eV.

4.3. The structural origin of the high force constant of iron in reduced rhyolitic glasses

Dauphas et al. (2014) used force constants measured in glasses with diverse $Fe^{3+}/\Sigma Fe$ to extrapolate the force constants to $Fe^{3+}/\Sigma Fe$ =0 and 1, and thus infer the force constants of the pure Fe^{2+} and Fe^{3+} end-members. With our revised data of $Fe^{3+}/\Sigma Fe$, we reappraise how iron redox state in magmas influences Fe isotopic fractionation. In Fig. 9, we plot the force constants of iron bonds as a function of the corrected $Fe^{3+}/\Sigma Fe$. From these, we estimate that the force constants of iron Fe^{2+} and Fe^{3+} are 193±7 and 364±23 N/m for basalt, andesite, dacite glasses (these samples form a single trend), and 250±11 and 382±31 N/m for rhyolite respectively. For comparison, Dauphas et al. (2014) had obtained force constants of 199±15, 351±29, 240±13, and 385±24 N/m for the same sample sets, which is similar to the values that we derive here with the corrected $\mathrm{Fe^{3+}}/\sum\mathrm{Fe}$ ratios. We therefore confirm the finding of Dauphas et al. (2014) that rhyolite glasses define a different trend than other samples. The force constant of Fe^{2+} in rhyolite is higher than those of Fe^{2+} in basalt, andesite, and dacite, whereas the force constants of Fe^{3+} in all compositions are indistinguishable.

The measurements made on the simple glass compositions help refine the structural and chemical origin of the peculiar behavior of Fe^{2+} in silicic magmas (Fig. 9). While the (Ca, Mg)-rich glass (CMS) has a force constant identical to those measured in basaltic glasses, a significant increase of <*F*> is observed in Na- and K-rich glasses. Furthermore, the force constant of the reduced KS4 glass matches the values observed for rhyolites, while NS4 has an intermediate <*F*> value (Fig. 9). This suggests that the control on the force constant may be related to the nature of the network-modifying cations present in the glass. Silica content may also potentially have an effect as seen by the weak correlations presented in the

supplementary material. However, we note in this respect that NS4 contains more silica than KS4 but still has a much lower <F> (only slightly higher than those of dacite and andesite). This suggests on the contrary that the silica content does not, per se, explain the higher force constant of Fe^{2+} in rhyolitic and alkali-rich glasses. Aluminum also typically plays pivotal and complex structural roles in silicate glasses and melts. A salient result of our study is to demonstrate that as far as NRIXS can tell, aluminum does not modify the structural role of iron (reduced and oxidized): simple Al-free glasses have strictly similar PDOS to Al-rich natural counter-parts. Finally, the fact that the highest force constant is found for glasses containing potassium as the dominant cation suggests that the ionic radius of the alkali cation has a direct effect on the force constant of iron.

A possible interpretation is that the large radius of K^+ (and Na+) lowers the average oxygen coordination number of Fe^{2+}. This interpretation is sustained by the detailed analysis of PDOS of simplified and natural compositions (Fig. 3). From the reduced CMS to reduced NS4 and KS4, the overall PDOS becomes broader with an increasing number of peaks and shoulders, this could be consistent with an increased number of iron environments at constant redox ratio. When ferric iron is introduced in the structure (i.e. sample prepared in air), the PDOS becomes even broader indicating also an increased number of iron geometries including IV-fold coordinated Fe^{3+} at around 85 meV (Fig. 3). Assuming that CMS IW is dominated by VI- and V-fold coordinated Fe^{2+}, as generally proposed for basic glasses (e.g. Jackson et al., 2005, Wilke et al., 2005; 2007, Le Losq et al. 2020), the Na-K substitution for Ca-Mg would trigger an increase of the fraction of IV-fold coordinated ferrous iron, at the expense of VI-fold coordinated iron and an overall decrease of the iron coordination number. This interpretation is furthermore consistent with XANES data and Mössbauer spectra. Though it is not possible to provide an average coordination number from our experimental results, we note that the normalized integrated pre-edge intensity (see the calibration of XANES spectra published in Le Losq et al., 2020) of the reduced rhyolite is 0.1975 whereas other similarly reduced glasses, intensities are comprised between 0.1816 and 0.1876 (Dauphas et al., 2014). Based on the coordination plot developed by Wilke et al. (2001) and adapted by LeLosq et al. (2020), these values imply that reduced rhyolite contains significant amount of IV-fold coordinated Fe^{2+} whereas other compositions contain Fe^{2+} in mixed V-fold and VI-fold coordinated iron. The fit to Mössbauer data also suggests that the overall coordination number of reduced rhyolite glass is lower than in other glasses (Fig. 10). Three lines were typically used to fit self-

680 consistently the data for the reduced glasses (IW series). Interestingly, these lines define 3
681 clusters within narrow ranges of IS and QS. It is tempting to attribute these lines to three
682 different sites occupied by ferrous iron (Fig. 10). From basaltic to rhyolitic glasses, each of
683 these sites show a systematic decrease of both IS and QS that may suggest a systematic
684 change of iron site symetries. We interpret the cluster exhibiting the lowest IS and QS to IV-
685 fold Fe^{2+} following a previous suggestion made on the similar samples by Solomatova et al.
686 (2017). The two other lines may be characteristic of V- and VI-fold sites or of another IV- and
687 a V-fold sites. The presence of a component, with low IS and QS, attributed to a four-fold
688 coordinated ferrous iron agrees with the interpretations of Rossano et al. (1999) of mössbauer
689 spectra of highly reduced tektites but also with Jackson et al., 2005; Solomatova et al. (2017)
690 and Berry et al. (2018). Most structural studies based on K-edge XANES have concluded that
691 Fe^{2+} in silicate glasses was mostly in V-fold coordination (e.g. Wilke et al., 2005; Giuli et al.,
692 2012; Fiege et al., 2017). Our conclusion slightly tempers this interpretation yet it does not
693 contradict the fact that the V-fold coordination of ferrous iron dominate over other
694 coordinations. Still, a significant amount of Fe^{2+} could actually occupy IV-fold coordinated sites
695 in silica-rich potassic and sodic glasses.
696
697

5. Concluding remarks

At equilibium, heavy isotopes are concentrated in the strongly bonded structural sites (Bigeleisen and Mayer, 1947; Schauble, 2004; Blanchard et al. 2017). The force constant can be influenced by several factors, notably the coordination number and geometry, redox state, and second neighbors (e.g. Blanchard et al. 2017, Rabin et al., 2021). In the case of Fe isotopes in igneous systems, oxygen fugacity has been shown to have a clear effect (Dauphas et al., 2014; Roskosz et al. 2015, Sossi and O'Neill, 2017). The effect of pressure was also pointed out (Shahar et al. 2016, Liu et al. 2017), influenced in part by spin transitions (Yang et al., 2019), though direct manifestation in nature of these effects are still elusive. Our study highlights the effect of iron coordination change at constant valence state. Decreasing the average coordination number of Fe^{2+} (from basalts to rhyolites) leads to a significant strengthening of the Fe-O bonds (observable from XANES, conventional Mössbauer spectroscopy and NRIXS) with <*F*> increasing from 193 to 250 N/m. This variation would be equivalent to a change in the oxidation state of Fe in a basalt from $Fe^{3+}/\Sigma Fe$ =0 to 0.33. It is a major driver of Fe isotopic fractionation during magmatic differentiation, explaining heavy isotopic compositions measuring in granitoids (Poitrasson and Freydier, 2005; Heimann et al., 2008; Telus et al., 2012; Sossi et al., 2012; Dauphas et al., 2014, Rabin et al. 2021).

In this study, we have for the first time combined NRIXS and conventional Mössbauer spectroscopy to determine the Lamb-Mössbauer factors of Fe^{2+} and $Fe3^{+}$ in a variety of silicate glasses of geological relevance. The same approach could be applied to other solid solutions where Fe^{2+} and Fe^{3+} can coexist (*e.g.,* garnet, biotite, Fe,Ti-oxides, clinopyroxene). Our approach yields a ratio between the recoil-free fractions of Fe^{3+} and Fe^{2+} of 1.21±0.06 (1s.d.) that can be applied to convert conventional Mössbauer spectra into $Fe^{3+}/\Sigma Fe$ in basalt, andesite, dacite, and rhyolite. We confirm that XANES-Mössbauer calibrations should consider some compositional specificities, notably in rhyolite with redox ratios ($Fe^{3+}/\Sigma Fe$) lower than 0.3. This unique behavior of rhyolites in XANES is also found in the form of high force constants of Fe^{2+}, high normalized integrated XANES pre-edge intensity and low IS and QS in Mössbauer spectra in rhyolite glass. These observations may point to a fraction of the total Fe^{2+} being IV-fold coordinated in rhyolite, as opposed to other compositions were Fe^{2+} is mostly in V- and VI-fold coordination. The structural control on this coordination anomaly is the high potassium/sodium content of rhyolites rather than the high silica or alumina content. We also

730 show that Fe-bonds in basalt and glass behave harmonically even at elevated temperature
731 relevant to metamorphism/crustal igneous systems. The use of room temperature
732 spectroscopic measurements to document high temperature geochemical equilibrium is thus
733 valid as long as no major phase transition are crossed. The question of the representativity of
734 solids (glasses or crystals) as proxies for liquids is still open but is obviously beyond the scope
735 of this study. Yet, we note that recent first-principle calculations demonstrate that a
736 congruent melting of a molten alloy would not lead to a significant change in the reduced
737 partition function ratios (Pinilla et al., 2021). A similar study needs to be carried for silicates
738 and melts of geological relevance.
739
740

6. Acknowledgements

This work was supported by NASA grants NNX17AE86G, NNX17AE87G, 80NSSC17K0744, 80NSSC20K0821 and NSF grant EAR-2001098 to ND. The extremely detailed, thoughtful and inspiring reviews from S.K Lee, H. O'Neill and two anonymous reviewers considerably improved this manuscript.

7. References

Andrault D., Muñoz M., Pesce G., Cerantola V., Chumakov A., Kantor I., Pascarelli S., Rüffer R. and Hennet L. (2018) Large oxygen excess in the primitive mantle could be the source of the Great Oxygenation Event. Geochem. Persp. Let. 6, 5-10.

Bancroft, M.G., and Brown, J.R. (1975) A Mössbauer study of coexisting hornblendes and biotites: quantitative Fe^{3+}/Fe^{2+} ratios. Am. Mineral. 60, 265–272.

Berry A.J., Stewart G.A., O'Neill H.St.C., Mallmann G. and Mosselmans J.F.W. (2018) A re-assessment of the oxidation state of iron in MORB glasses. Earth Planet. Sci. Lett. 483, 114-123.

Berry A.J., O'Neill H.St.C., Jayasuriya K., Campbell S. and Foran G. (2003) XANES calibrations for the oxidation state of iron in a silicate glass. Am. Mineral. 88, 967–977.

Bézos A., Lorand J.-P., Humler E. and Gros M. (2005) Platinum-group element systematics in Mid-Oceanic Ridge basaltic glasses from the Pacific, Atlantic, and Indian Oceans. Geochim. Cosmochim. Acta 69, 2613–2627.

Bézos A. and Humler E. (2005) The $Fe^{3+}/\Sigma Fe$ ratios of MORB glasses and their implications for mantle melting. Geochim. Cosmochim. Acta 69 (3), 711–725.

Bigeleisen J. and Mayer M.G. (1947) Calculation of Equilibrium Constants for Isotopic Exchange Reactions. Journal of Chemical Physics, 15, 261.

Blanchard M., Balan E., Schauble E.A. (2017) Equilibrium fractionation of non-traditional isotopes: A molecular modeling perspective. Reviews in Mineralogy and Geochemistry 82, 27-63

Borisov A. and McCammon C. (2010) The effect of silica on ferric/ferrous ratio in silicate melts: An experimental study using Mössbauer spectroscopy. Am. Mineral. 95, 545–555.

Borisov A., Behrens H. and Holtz F. (2017) Effects of strong network modifiers on Fe^{3+}/Fe^{2+} in silicate melts: an experimental study. Contrib. Mineral. Petrol. 172, 34.

Bouhifd M.A., Andrault D., Fiquet G. and Richet P. (1996) Thermal expansion of forsterite up to the melting point. Geophys. Res. Let. 23, 1143-1146.

Canil D. and O'Neill H.St.C. (1995) Distribution of ferric iron in some upper-mantle assemblages. J. Pet. 37, 609-635.

Carmichael I.S.E. (1991) The redox states of basic and silicic magmas: a reflection of their source regions? Contrib. Mineral. Petrol. 106, 129–141.

Chen Y.-L. and Yang D.-P. (2007) Mössbauer Effect in Lattice Dynamics: Experimental Techniques and Applications. John Wiley & Sons.

Christie D.M., Carmichael, I.S.E. and Langmuir C.H. (1986) Oxidation states of mid-ocean ridge basalt glasses. Earth Planet. Sci. Lett. 79, 397–411.

Chumakov A. and Sturhahn W. (1999) Experimental aspects of inelastic nuclear resonance scattering. Hyperfine interactions 123, 781-808.

Cottrell E. and Kelley K. A. (2011) The oxidation state of Fe in MORB glasses and the oxygen fugacity of the upper mantle. Earth Planet. Sci. Lett. 305, 270–282.

Cottrell E., Kelley K. A., Lanzirotti A. and Fischer R. A. (2009) High-precision determination of iron oxidation state in silicate glasses using XANES. Chem. Geol. 268, 167–179.

Dauphas N., Hu M. Y., Baker E. M., Hu J., Tissot F. L., Alp E. E., Roskosz M., Zhao J., Bi W. and Liu J. (2018) SciPhon: a data analysis software for nuclear resonant inelastic X-ray scattering with applications to Fe, Kr, Sn, Eu and Dy. J. Synch. Rad. 25, 1581–1599.

Dauphas N., Roskosz M., Alp,E.E., Golden D.C., Sio C.K., Tissot F.L.H., Hu M.Y., Zhao J., Gao L. and Morris R.V. (2012) A general moment NRIXS approach to the determination of equilibrium Fe isotopic fractionation factors: application to goethite and jarosite. Geochim. Cosmochim. Acta 94, 254–275.

Dauphas N., Roskosz M., Alp E.E., Neuville D.R., Hu M.Y., Sio C.K., Tissot F.L.H., Zhao J., Tissandier L., Médard E. and Cordier C. (2014) Magma redox and structural controls on iron isotope variations in Earth's mantle and crust. Earth Planet. Sci. Lett. 398, 127–140.

De Grave E. and Van Alboom A. (1991) Evaluation of ferrous and ferric Mössbauer fractions. Phys. Chem. Miner. 18, 337–342.

De Grave E., Verbeeck A.E. and Chambaere D.G. (1985) Influence of small aluminum substitutions on the hematite lattice. Physics Letters A, 107, 181–184.

Dingwell D.B. (1991) Redox viscometry of some Fe-bearing silicate melts. Am. Mineral. 76, 1560–1562.

Dyar M. D., Naney M. T. and Swanson S. E. (1987) Effects of quench methods on Fe^{3+}/Fe^{2+} ratios: A Mössbauer and wet-chemical study. Am. Mineral. 72, 792–800.

Dyar M., Agresti D., Schaefer M., Grant C. and Stlute E. (2006) Mössbauer spectroscopy of Earth and planetary materials. Annu. Rev. Earth Planet. Sci. 34, 83–125.

Dyar M.D., Breves E.A., Emerson E., Bell S.W., Nelms M., Ozanne M.V., Peel S.E., Carmosino M.L., Tucker J.M., Gunter M.E., Delaney J.S., Lanzirotti A. and Woodland A.B. (2012) Accurate determination of ferric iron in garnets by bulk Mössbauer spectroscopy and synchrotron micro-XANES. Am. Mineral. 97, 1726–1740.

Farges F., Lefrere Y., Rossano S., Berthereau A., Calas G., and Brown G.E. Jr. (2004) The effect of redox state on the local structural environment of iron in silicate glasses: a combined XAFS spectroscopy, molecular dynamics, and bond valence study. J. Non-cryst. Solids, 344, 176-188.

Fiege A., Ruprecht P., Simon A.C., Bell A.S., Göttlicher J., Newille M., Lanzirotti T. and Moore G. (2017) Calibration of Fe XANES for high-precision determination of Fe oxidation state in glasses: Comparison of new and existing results obtained at different synchrotron radiation sources. Am. Mineral. 102, 369-380.

Gaillard F., Scaillet B. and Arndt N. (2011) Atmospheric oxygenation caused by a change in volcanic degassing pressure. Nature. 478, 229-32.

Giuli G., Pratesi G., Cipriani C., and Paris E. (2002) Iron local structure in tektites and impact glasses by extended X-ray absorption fine structure and high-resolution X-ray absorption near-edge structure spectroscopy. Geochim. Cosmochim. Acta, 66, 4347-4353.

Giuli G., Alonso-Mori R., Cicconi M.R., Paris E., Glatzel P., Eeckhout S.G. and Scaillet B. (2012) Effect of alkalis on the Fe oxidation state and local environment in peralkaline rhyolitic glasses. Am. Mineral. 97, 468–475.

Heimann A., Beard B.L. and Johnson C.M. (2008) The role of volatile exsolution and sub-solidus fluid/rock interactions in producing high $^{56}Fe/^{54}Fe$ ratios in siliceous igneous rocks. Geochim. Cosmochim. Acta 72, 4379-4396.

Hu M.Y., Toellner T.S., Dauphas N., Alp E.E. and Zhao J. (2013) Moments in nuclear resonant inelastic x-ray scattering and their applications. Phys. Rev. B 87, 064301.

Jackson J.M., Sturhahn W., Lerche M., Zhao J., Toellner T.S., Alp E.E., Sinogeikin S.V., Bass J.D., Murphy C.A. and Wicks J.K. (2013) Melting of compressed iron by monitoring atomic dynamics. Earth Planet. Sci. Lett. 362, 143-150.

Jackson W.E., Farges F., Yeager M., Mabrouk P.A., Rossano S., Waychunas G.A., Solomon E.A. and Brown G.E. Jr. (2005) Spectroscopic study of Fe(II) in silicate glasses: implications for the coordination environment of Fe(II) in anhydrous silicate melts of geochemical interest. Geochim. Cosmochim. Acta 69, 4315-4332.

Jayasuriya K.D., O'Neill H.S.C., Berry A.J. and Campbell S.J. (2004) A Mössbauer study of the oxidation state of Fe in silicate melts. Am. Mineral. 89, 1597–1609.

Kelley K.A. and Cottrell E. (2009) Water and the oxidation state of subduction zone magmas. Science, 325, 605–607.

Kennedy G.C. (1948) Equilibrium between volatiles and iron oxides in igneous rocks. Am. J. Sci. 246, 529–549.

Kress V. and Carmichael I. (1991) The compressibility of silicate liquids containing Fe_2O_3 and the effect of composition, temperature, oxygen fugacity and pressure on their redox states. Contrib. Miner. Petrol. 108, 82–92.

Kress V.C. and Carmichael I.S.E. (1988) Stoichiometry of the iron oxidation reaction in silicate melts. Am. Mineral. 73, 1267–1274.

Kump L.R., Kasting J.F. and Barley M.E. (2001) Rise of atmospheric oxygen and the "upside-down" Archean mantle, Geochem. Geophys. Geosyst., 2, 1025.

Lange R.A. and Carmichael I.S.E. (1989) Ferric-ferrous equilibria in Na_2O-FeO-Fe_2O_3-SiO_2 melts-effects of analytical techniques on derived partial molar volumes. Geochim. Cosmochim. Acta 53, 2195–2204.

Le Losq Ch., Moretti R., Oppenheimer C. and Neuville D.R. (2020) Coupled Fe^{2+} / Fe^{3+} and CN changes in magmatic melts revealed by Fe K-edge XANES spectroscopy – application at the Erebus volcano. Contrib. Miner. Petrol. 175, 64-77.

Liu J., Dauphas N., Roskosz M., Hu M. Y., Yang H., Bi W., Zhao J., Alp E. E., Hu J. Y. and Lin J.-F. (2017) Iron isotopic fractionation between silicate mantle and metallic core at high pressure. Nature Com. 8, 1–6.

Moretti R. (2005) Polymerisation, basicity, oxidation state and their role in ionic modelling of silicate melts. Ann. Geophys. 48, 583– 608.

Mysen B.O. and Frantz J.D. (1992) Raman spectroscopy of silicate melts at magmatic temperatures: Na_2O-SiO_2, K_2O-SiO_2 and Li_2O-SiO_2 binary compositions in the temperature range 25°- 1475°C. Chem. Geol. 96, 321-332.

Mysen B.O. and Virgo D. (1985) Iron-bearing silicate melts: relations between pressure and redox equilibria. Phys. Chem. Miner. 12, 191–200.

Mysen B. and Richet P. (2005) Silicate Glasses and Melts: Properties and Structure. Elsevier.

Neuville D.R. and Mysen B.O. (1996) Role of aluminium in the silicate network: In situ, high-temperature study of glasses and melts on the join SiO_2-$NaAlO_2$. Geochim. Cosmochim. Acta, 60, 1727-1737.

Neuville D.R., Hennet L., Florian P. and de Ligny D. (2014) In situ High-Temperature Experiments. Rev. Miner. Geochem. 78, 779–800.

Nie N.X., Dauphas N., Alp E.E., Zeng H., Sio C.K., Hu J.Y., Chen X., Aarons S.M., Zhang Z., Tian H.-C., Wang D., Prissel K.B., Greer J., Bi W., Hu M.Y., Zhao J., Shahar A. Roskosz M., Teng F.-Z., Krawczynski M.J., Heck P.R. and Spear F.S. (2021) Iron, magnesium, and titanium isotopic fractionations between garnet, ilmenite, fayalite, biotite, and tourmaline: results from NRIXS, ab initio, and study of mineral separates from the Moosilauke metapelite. Geochim. Cosmochim. Acta 302, 18-45.

Niemantsverdriet J.W., Van der Kraan A.M. and Delgass W.N. (1984) Characterization of surface phases in bimetallic $FeRhSiO_2$ catalysts by in situ Mössbauer spectroscopy at cryogenic temperatures. Journal of Catalysis, 89, 138–149.

O'Neill H.St.C., Berry A.J., McCammon C., Jayasuriya K.D., Campbell S.J. and Foran G. (2006) An experimental determination of the effect of pressure on the $Fe^{3+}/\sum Fe$ ratio of an anhydrous silicate melt to 3.0 GPa. Am. Mineral. 91, 404–412.

Pinilla C., de Moya A., Rabin, S., Morard G., Roskosz M. and Blanchard M. (2021) First-principles investigation of equilibrium iron isotope fractionation in $Fe_{1-x}S_x$ alloys at Earth's core formation conditions. Earth Planet. Sci. Lett. (In Rev.)

Poitrasson F. and Freydier R. (2005) Heavy iron isotope composition of granites determined by high resolution MC-ICP-MS. Chem. Geol. 222, 132-147.

Rabin S., Blanchard M., Pinilla C., Poitrasson, F. and Grégoire M. (2021) First-principles calculation of iron and silicon isotope fractionation between Fe-bearing minerals at magmatic temperatures: The importance of second atomic neighbors. Geochim. Cosmochim. Acta 304, 101-118.

Richet P., Roskosz M. and Roux J. (2006) Glass formation in silicates: Insights from composition. Chem. Geol. 225, 388-401.

Righter K. (2013) Redox systematics of martian magmas with implications for magnetite stability. Am. Mineral. 98, 616–628.

Roskosz M., Sio C.K., Dauphas N., Bi W., Tissot F.L.H., Hu M.Y., Zhao J. and Alp E.E. (2015) Spinel–olivine–pyroxene equilibrium iron isotopic fractionation and applications to natural peridotites. Geochim. Cosmochim. Acta 169, 184–199.

Roskosz M., Toplis M.J. and Neuville D.R. (2008) Quantification of the kinetics of iron oxidation in silicate melts using Raman spectroscopy and assessment of the role of oxygen diffusion. Am. Mineral. 93, 1749–1759.

Rossano S., Balan E., Morin G., Bauer J.-P., Calas G. and Brouder C. (1999) ^{57}Fe Mössbauer spectroscopy of tektites. Phys. Chem. Minerals 26, 530-538.

Rossano S., Behrens H. and Wilke M. (2008) Advanced analyses of ^{57}Fe Mössbauer data of aluminosilicate glasses. Phys. Chem. Miner. 35, 77–93.

Schauble E.A. (2004) Applying stable isotope fractionation theory to new systems. Reviews in Mineralogy and Geochemistry 55, 65-111.

Seto M., Yoda Y., Kikuta S., Zhang X. W. and Ando M. (1995) Observation of nuclear resonant scattering accompanied by phonon excitation using synchrotron radiation. Physical review letters 74, 3828.

Shahar A., Schauble E.A., Caracas R., Gleason A.E., Reagan M.M., Xiao Y., Shu J. and Mao W. (2016) Pressure-dependent isotopic composition of iron alloys. Science 352, 580–582.

Sio C.K., Roskosz M., Dauphas N., Bennett N.R., Mock T. and Shahar A. (2018) The isotope effect for Mg-Fe interdiffusion in olivine and its dependence on crystal orientation, composition and temperature. Geochim. Cosmochim. Acta 239, 463-480.

Solomatova, N.V., Jackson J.M., Sturhahn, W., Rossman, G.R., and Roskosz, M. (2017) Electronic environments of ferrous iron in rhyolitic and basaltic glasses at high pressure. J. Geophys. Res. Solid Earth, 122, 6306-6322.

Sossi P.A. and O'Neill H.St.C. (2017) The effect of bonding environment on iron isotope fractionation between minerals at high temperature. Geochim. Cosmochim. Acta 196, 121–143.

Sossi P.A., Foden, J.D. and Halverson G.P. (2012) Redox-controlled iron isotope fractionation during magmatic differentiation: an example from the Red Hill intrusion, S. Tasmania. Contrib. Miner. Petrol. 164, 757-772.

Stolper D.A. and Bucholz C.E. (2019) Neoproterozoic to early Phanerozoic rise in island arc redox state due to deep ocean oxygenation and increased marine sulfate levels. PNAS; 116, 8746-8755.

Sturhahn W., Toellner T.S., Alp E.E., Zhang X., Ando M., Yoda Y., Kikuta S., Seto M., Kimball C.W. and Dabrowski B. (1995) Phonon Density of States Measured by Inelastic Nuclear Resonant Scattering. Phys. Rev. Letters 74, 3832.

Telus M., Dauphas N., Moynier F., Tissot F.L.H., Teng F.-Z., Nabelek P.I., Craddock P.R. and Groat L.A. (2012) Iron, zinc, magnesium and uranium isotopic fractionation during continental crust differentiation: The tale from migmatites, granitoids, and pegmatites. Geochim. Cosmochim. Acta 97, 247–265.

Weigel C., Mccammon C. and Keppler H. (2010) High-temperature Mössbauer spectroscopy: A probe for the relaxation time of Fe species in silicate melts and glasses. Am. Mineral. 95, 1701-1707.

Westre T.E., Kennepohl P., DeWitt J.G., Hedman B., Hodgson K.O. and Solomon E.I. (1997) A multiplet analysis of Fe K-edge 1s - 3d pre-edge features of iron complexes. J. Amer. Chem. Society, 119, 6297 - 6314.

Wilke M., Partzsch G.M., Bernhardt R. and Lattard D. (2005) Determination of the iron oxidation state in basaltic glasses using XANES at the K-edge. Chem. Geol. 220, 143–161.

Wilke M., Farges F., Petit P.-E., Brown Jr. G.E. and Martin F. (2001) Oxidation state and coordination of Fe in minerals: An Fe K-XANES spectroscopic study. Am. Mineral. 86, 714–730.

Wilke M., Farges F., Partzsch G.M., Schmidt C. and Behrens H. (2007) Speciation of iron in silicate glasses and melts by in-situ XANES spectroscopy. Am. Mineral. 92, 44-56.

Woodland A.B. and Ross, C.R. II (1994) A crystallographic and Mössbauer spectroscopy study of $Fe_3^{2+}Al_2Si_3O_{12}$-$Fe_3^{2+}Fe_2^{3+}Si_3O_{12}$, (almandine-"skiagite") and $Ca_3Fe_3^{2+}Si_3O_{12}$-$Fe_3^{2+}Fe_3^{2+}Si_3O_{12}$ (andradite-"skiagite") garnet solid solutions. Phys. Chem. Min. 21, 117–132.

Zhang H. L., Hirschmann M. M., Cottrell E., Newville M. and Lanzirotti A. (2016) Structural environment of iron and accurate determination of $Fe^{3+}/\sum Fe$ ratios in andesitic glasses by XANES and Mössbauer spectroscopy. Chem. Geol. 428, 48–58.

Zhang H.L., Solheid P.A., Lange R.A., Von Der Handt A. and Hirschmann M.M. (2015) Accurate determination of $Fe^{3+}/\sum Fe$ of andesitic glass by Mössbauer spectroscopy. Am. Mineral. 100, 1967–1977.

1043 Table 1: Glass compositions determined by EMPA (Wt%) (Dauphas et al. 2014; this study)

1044

Name	SiO2	Al2O3	FeO	CaO	MgO	Na2O	K2O	TiO2
Tholeitic Basalt Air	45.8	14.5	7.7	11.2	18.0	1.3	0.0	0.9
Tholeitic Basalt Int	45.7	14.4	7.7	11.3	18.1	1.5	0.1	0.8
Tholeitic Basalt IW	46.3	14.5	7.6	11.4	18.3	1.0	0.1	0.9
Basalt Air	50.5	16.7	7.6	12.7	9.4	1.9	0.0	1.0
Basalt Int	49.9	16.6	7.6	12.6	9.3	2.2	0.0	1.0
Andesite Air	55.4	16.1	7.0	6.9	8.1	3.3	1.5	0.8
Andesite Int	55.3	16.1	7.1	7.1	8.3	3.2	1.5	0.8
Andesite IW	55.8	16.3	7.0	7.2	8.3	3.0	1.4	0.8
Dacite Air	63.8	14.9	4.5	4.8	4.3	3.9	2.5	0.7
Dacite Int	63.4	14.9	4.6	4.8	4.3	3.8	2.5	0.7
Dacite IW	64.1	14.9	4.5	4.7	4.2	3.9	2.5	0.7
Rhyolite Air	75.5	10.5	4.1	0.0	0.0	5.0	4.6	0.0
Rhyolite Int	75.7	10.4	4.1	0.0	0.0	5.3	4.7	0.0
Rhyolite IW	75.7	10.4	4.1	0.0	0.0	4.5	4.5	0.0
CMS air	59.6	0.0	6.6	20.7	11.4	0.0	0.0	0.0
CMS IW	59.4	0.0	6.9	20.5	11.5	0.0	0.0	0.0
KS4 Air	65.5	0.0	8.3	0.0	0.0	0.0	25.9	0.0
KS4 IW	65.7	0.0	8.2	0.0	0.0	0.0	25.5	0.0
NS4 air	76.3	0.0	11.2	0.0	0.0	12.4	0.0	0.0
NS4 IW	76.6	0.0	10.9	0.0	0.0	11.9	0.0	0.0

1045

1046

Table 2: Isomer shifts (IS), quadrupole splitting (QS) and associated standard deviation, all in mm/s, of the components used to fit the ^{57}Fe Mössbauer spectra presented in Figure 2.

Sample		Reduced (IW)					Oxidized (Air)				
		IS	IS err	QS	Qs err	band area	IS	IS err	QS	Qs err	band area
NS4	site #1	1.016	0.000	1.877	0.000	[illegible]	0.267	0.001	0.968	0.002	78.2
	site #2	0.646	0.001	1.623	0.001	[illegible]	1.076	0.003	1.820	0.005	21.8
	site #3	1.388	0.001	1.671	0.001	[illegible]					
KS4	site #1	1.007	0.001	1.605	0.007	[illegible]	0.262	0.001	0.852	0.001	79.2
	site #2	1.051	0.001	2.221	0.003	[illegible]	1.031	0.003	1.952	0.006	20.8
CMS	site #1	1.162	0.001	1.928	0.001	[illegible]	0.568	0.002	1.060	0.004	54.4
	site #2	0.815	0.001	1.814	0.001	[illegible]	0.856	0.002	2.657	0.003	40.1
							1.614	0.005	1.887	0.007	5.5
Tholeiitic Basalt at 90	site #1	1.170	0.002	2.048	0.009	[illegible]	0.510	0.023	1.424	0.007	40.0
	site #2	1.083	0.004	1.391	0.013	[illegible]	1.135	0.007	2.062	0.007	40.1
	site #3	1.209	0.002	2.680	0.010	[illegible]	0.200	0.015	1.449	0.008	14.5
	site #4						1.577	0.009	1.967	0.012	5.5
Tholeiitic Basalt at 5	site #1	1.180	0.002	2.049	0.012	[illegible]					
	site #2	1.107	0.006	1.369	0.020	[illegible]					
	site #3	1.225	0.003	2.703	0.014	[illegible]					
Andesite at 90K	site #1	1.165	0.003	1.977	0.013	[illegible]					
	site #2	1.214	0.004	2.614	0.017	[illegible]					
	site #3	1.075	0.007	1.317	0.018	[illegible]					
Dacite at 90K	site #1	1.165	0.002	1.952	0.009	[illegible]					
	site #2	1.071	0.005	1.293	0.015	[illegible]					
	site #3	1.220	0.003	2.609	0.011	[illegible]					
Rhyolite at 90K	site #1	1.155	0.001	1.897	0.005	[illegible]					
	site #2	1.046	0.002	1.162	0.007	[illegible]					
	site #3	1.211	0.002	2.615	0.005	[illegible]					

Table 3: Compilation of parameters derived from NRIXS spectra collected at room temperature on simple model glasses. The data reduction was done using the SciPhon software (Dauphas et al. 2018).

	CMS-AIR			CMS-IW			KS4-AIR			KS4-IW			NS4-AIR			NS4-IW		
Total energy range:	-157.52	to	176.41	-158.64	to	177.28	-157.91	to	176.50	-160.60	to	178.36	-158.67	to	176.88	-159.03	to	177.52
Energy cutoff (left and right in meV):	61	and	32	49	and	29	57	and	22	80	and	36	59	and	25	67	and	41
Baseline subtracted:		linear			linear			linear			linear			linear			linear	
a=	1.51E-03	±	7.05E-04	1.44E-03	±	8.63E-04	2.42E-03	±	6.32E-04	5.86E-05	±	3.49E-04	1.81E-03	±	7.30E-04	1.16E-03	±	6.30E-04
b=	6.47E-01	±	9.91E-02	8.53E-01	±	1.26E-01	5.74E-01	±	8.93E-02	4.03E-01	±	4.75E-02	7.17E-01	±	1.03E-01	6.23E-01	±	8.80E-02
Input temperature (K):	302			302			302			300			302			302		
Temperature from detailed balance (K):	309			304			311			295			322			311		
----------From 5----------																		
lamb-mossbauer factor from 5:	0.6794	±	0.0014	0.6302	±	0.0012	0.6570	±	0.0015	0.5510	±	0.0026	0.6598	±	0.0015	0.5756	±	0.0017
Mean square displacement <z^2> from 5 (A^2):	7.25E-03	±	2.89E-05	8.66E-03	±	2.69E-05	7.88E-03	±	3.10E-05	1.12E-02	±	6.52E-05	7.80E-03	±	3.19E-05	1.04E-02	±	4.01E-05
Internal energy/atom from 5 (meV):	29.81	±	0.64	28.77	±	0.60	30.69	±	0.66	29.07	±	0.72	30.59	±	0.69	28.97	±	0.63
Kinetic energy/atom from 5 (meV):	14.90	±	0.32	14.38	±	0.30	15.34	±	0.33	14.53	±	0.36	15.29	±	0.35	14.48	±	0.32
Force constant from 5 (N/m):	280	±	11	201	±	9	349	±	14	236	±	17	341	±	15	214	±	10
----------beta-value coefficients from 5----------																		
1000 ln beta 56Fe/54Fe=A1/T^2+A2/T^4+A3/T6 (T in K)																		
A1:	7.994E+05	±	3.196E+04	5.737E+05	±	2.488E+04	9.953E+05	±	3.925E+04	6.742E+05	±	4.886E+04	9.724E+05	±	4.169E+04	6.118E+05	±	2.727E+04
A2:	-7.22E+09	±	7.18E+08	-4.75E+09	±	6.21E+08	-1.02E+10	±	9.95E+08	-6.30E+09	±	1.38E+09	-9.86E+09	±	1.09E+09	-4.42E+09	±	5.57E+08
A3:	1.81E+14	±	3.30E+13	1.36E+14	±	3.21E+13	2.75E+14	±	5.15E+13	1.91E+14	±	7.05E+13	2.72E+14	±	5.74E+13	9.18E+13	±	2.35E+13
1000 ln beta 56Fe/54Fe=B1<F>/T2-B2<F>^2/T^4 (T in K)																		
B1:	2853			2853			2853			2853			2853			2853		
B2:	67104			81050			59210			75976			59604			74524		
----------From 3----------																		
lamb-mossbauer factor from 3:	0.6701			0.6259			0.6402			0.5289			0.6459			0.5532		
Mean square displacement <z^2> (A^2):	7.51E-03			8.79E-03			8.37E-03			1.20E-02			8.20E-03			1.11E-02		
d<z^2>/dT (A^2/K):	2.34E-05			2.76E-05			2.63E-05			3.85E-05			2.57E-05			3.55E-05		
Critical temperature (K):	801			679			714			488			729			528		
Resilience (N/m):	59			50			53			36			54			39		
Internal energy/atom from 3 (meV):	29.83			28.77			30.73			29.17			30.63			29.03		
Kinetic energy/atom from 3 (meV):	14.91			14.39			15.37			14.59			15.32			14.52		
Vibrational entropy (kb/atom):	1.12			1.26			1.04			1.22			1.05			1.25		
Helmholtz free energy (meV):	0.67			-4.09			3.66			-2.34			3.38			-3.39		
Vibrational specific heat (kb/atom):	0.88			0.91			0.85			0.89			0.85			0.90		
lamb-mossbauer factor at T=0 from 3:	0.9072			0.8954			0.9100			0.8914			0.9101			0.8917		
Kinetic energy/atom at T=0 from 3 (meV):	7.51			6.30			8.41			6.79			8.32			6.55		
Force constant from 3 (N/m):	280			201			349			237			341			215		
----------beta-value coefficients from 3----------																		
1000 ln beta 56Fe/54Fe=A1/T^2+A2/T^4+A3/T6 (T in K)																		
A1:	7.996E+05			5.739E+05			9.955E+05			6.749E+05			9.728E+05			6.124E+05		
A2:	-7.23E+09			-4.75E+09			-1.02E+10			-6.32E+09			-9.88E+09			-4.43E+09		
A3:	1.83E+14			1.37E+14			2.78E+14			1.93E+14			2.75E+14			9.26E+13		

Table 4: Redox ratios (as determined from conventional Mössbauer spectroscopy at 300K, data from Dauphas et al., 2014) and corrected for the recoil-free fractions of ferrous and ferric irons), Lamb-Mössbauer factors and force constants calculated from NRIXS spectra and C derived from the same spectra. The values of *f2*, *f3*, and C were obtained by combining NRIXS and conventional Mössbauer data (see text for details).

Sample	*"Raw"* redox ratio			*fLM*			*f2*			*f3*			*C*			Corrected redox ratio			*<F>* (N/m)		
tholeiitic basalt IW	0	±	0.02	0.5956	±	0.0016										0.00	±	0.03	188	±	7
tholeiitic basalt INT	0.4	±	0.02	0.6527	±	0.0026	0.5954	±	0.0056	0.7676	±	0.0159	1.289	±	0.036	0.34	±	0.07	227	±	15
tholeiitic basaltAIR	0.54	±	0.02	0.6784	±	0.0025										0.48	±	0.06	281	±	18
basalt INT	0.32	±	0.02	0.6330	±	0.0029	0.5947	±	0.0115	0.7335	±	0.0195	1.233		0.056	0.28	±	0.09	250	±	23
Basalt AIR	0.57	±	0.03	0.6666	±	0.0027										0.52	±	0.08	275	±	17
Andesite IW	0	±	0.02	0.5967	±	0.0016										0.00	±	0.03	199	±	11
Andesite Int	0.35	±	0.02	0.6289	±	0.0018	0.5968	±	0.0038	0.6978	±	0.0101	1.169	±	0.023	0.32	±	0.08	254	±	16
Andesite AIR	0.55	±	0.02	0.6482	±	0.0018										0.51	±	0.05	283	±	17
Dacite IW	0	±	0.02	0.5765	±	0.0028										0.00	±	0.03	197	±	13
Dacite INT	0.32	±	0.02	0.6104	±	0.0026	0.5793	±	0.0041	0.6672	±	0.0095	1.152	±	0.022	0.29	±	0.08	266	±	19
Dacite AIR	0.59	±	0.02	0.6242	±	0.0029										0.56	±	0.05	283	±	21
Rhyolite IW	0	±	0.05	0.5342	±	0.0021										0.00	±	0.03	251	±	10
Rhyolite INT	0.51	±	0.03	0.5740	±	0.0027	0.5304	±	0.0043	0.6374	±	0.0076	1.202	±	0.022	0.46	±	0.08	307	±	16
Rhyolite AIR	0.73	±	0.03	0.6078	±	0.0023										0.69	±	0.06	346	±	20
NS4 IW	0	±	0.02	0.5756	±	0.0017										0.00	±	0.03	214	±	10
NS4 AIR	0.78	±	0.02	0.6598	±	0.0015	0.5756	±	0.0040	0.6882	±	0.0067	1.196	±	0.017	0.75	±	0.04	341	±	15
KS4 IW	0	±	0.02	0.5510	±	0.0026										0.00	±	0.03	236	±	17
KS4 AIR	0.79	±	0.02	0.6570	±	0.0015	0.5510	±	0.0041	0.6924	±	0.0066	1.257	±	0.018	0.75	±	0.04	349	±	14
CMS IW	0	±	0.02	0.6302	±	0.0012										0.00	±	0.03	201	±	9
CMS AIR	0.58	±	0.02	0.6794	±	0.0014	0.6302	±	0.0041	0.7201	±	0.0098	1.143	±	0.019	0.55	±	0.05	280	±	11

Table 5: Parameters derived from NRIXS analyses of olivine (100%Fe^{2+}) and basaltic glass synthesized in air (57%Fe^{3+}+43%Fe^{2+}) for different temperatures. Only partial results are presented for the 1223K olivine measurement because of the large mutiphonon contribution at high temperature.

	Basalt air			Basalt air			Basalt air			Olivine			Olivine			Olivine			Olivine		
Temperature (K)	300			558			773			300			300			773			1223		
Values calculated from S(E)																					
Lamb-Mössbauer factor from S	0.685	±	0.002	0.508	±	0.003	0.375	±	0.002	0.757	±	0.003	0.769	±	0.003	0.476	±	0.004	0.226	±	0.007
Mean square displacement $<z^2>$ from S (Å^2)	0.00711	±	0.00004	0.01271	±	0.00009	0.01842	±	0.00009	0.00523	±	0.00005	0.00493	±	0.00005	0.01395	±	0.00013	0.02790	±	0.00047
Internal energy/atom from S (meV)	29.91	±	0.71	50.23	±	1.44	68.26	±	1.64	28.67	±	0.72	29.15	±	0.91	67.65	±	1.82	105.80	±	2.80
Kinetic energy/atom from S (meV)	14.96	±	0.36	25.12	±	0.72	34.13	±	0.82	14.33	±	0.36	14.57	±	0.46	33.82	±	0.91	52.90	±	1.40
Force constant from S (N/m)	298	±	16	276	±	23	291	±	31	202	±	15	245	±	30	181	±	38			
$1000\ln(b^{56}Fe/^{54}Fe)=A_1/T^2+A_2/T^4+A_3/T^6$ (T in K)																					
A_1	8.512E+05	±	4.635E+04	7.877E+05	±	6.427E+04	8.292E+05	±	8.857E+04	5.763E+05	±	4.182E+04	6.998E+05	±	8.419E+04	5.171E+05	±	1.080E+05			
A_2	-7.4E+09	±	1.0E+09	-5.4E+09	±	1.1E+09	-6.8E+09	±	2.4E+09	-3.5E+09	±	7.0E+08	-7.7E+09	±	2.5E+09	-1.7E+09	±	1.9E+09			
A_3	1.6E+14	±	4.2E+13	7.6E+13	±	3.3E+13	1.2E+14	±	1.1E+14	6.7E+13	±	2.1E+13	2.7E+14	±	1.2E+14	7.5E+12	±	5.8E+13			
1000ln(beta56Fe/54Fe)=B1<F>/T2-B2<F>^2/T^4 (T in K)																					
B_1	2853			2853			2853			2853			2853			2853					
B_2	63910			59983			64907			68662			79161			48845					
Values calculated from g(E)																					
Lamb-Mössbauer factor from g	0.679			0.505			0.367			0.756			0.768			0.473					
Mean square displacement $<z^2>$ from g (Å^2)	0.00727			0.01283			0.01880			0.00525			0.00495			0.01405					
$d<z^2>/dT$ (Å^2/K)	2.20E-05			2.22E-05			2.35E-05			1.60E-05			1.49E-05			1.80E-05					
Critical temperature (K)	853			845			797			1175			1258			1041					
Resilience (N/m)	63			62			59			86			93			77					
Internal energy/atom from g (meV)	30			50			68			29			29			68					
Kinetic energy/atom from g (meV)	15			25			34			14			15			34					
Vibrational entropy (kb/atom)	1.08			1.64			1.97			1.12			1.10			2.04					
Helmholtz free energy (meV)	2.12			-28.50			-62.61			-0.28			0.76			-68.35					
Vibrational specific heat (kb/atom)	0.87			0.96			0.98			0.90			0.89			0.98					
lamb-mossbauer factor at T=0 from g	0.91			0.91			0.91			0.91			0.92			0.91					
Kinetic energy/atom at T=0 from g (meV)	7.81			7.69			7.74			6.73			7.09			6.55					
Force constant from g (N/m)	298			277			291			202			245			181					
$1000\ln(b^{56}Fe/^{54}Fe)=A_1/T^2+A_2/T^4+A_3/T^6$ (T in K)																					
A_1	851630			789786			830871			576734			700143			517396					
A_2	-7.41E+09			-5.50E+09			-6.83E+09			-3.55E+09			-7.75E+09			-1.66E+09					
A_3	1.61E+14			8.59E+13			1.25E+14			6.99E+13			2.80E+14			5.35E+12					
Input density (g/cc)	2.78			2.78			2.78			3.43			3.43			3.43					
Input bulk modulus (GPa)	100			100			63			100			129			100					
Debye velocity (m/s)	3897	±	127	3566	±	79	3511	±	58	4924	±	254	5367	±	208	4405	±	167			
p-wave velocity (m/s)	7210	±	78	7021	±	46	5983	±	38	7453	±	188	8296	±	150	7073	±	116			
s-wave velocity (m/s)	3466	±	121	3162	±	75	3139	±	55	4449	±	242	4839	±	198	3957	±	159			
Poisson ratio	0.35			0.37			0.31			0.22			0.24			0.27					
Comparison 1000ln(b) at 300K																					
from A_1-A_3 coefficients (‰)	8.76			2.48			1.37			6.06			7.20			0.86					
from A_1-A_3 β coefficients (‰)	8.77			2.48			1.37			6.07			7.21			0.86					
from kinetic energy (‰)	8.72			2.48			1.37			6.05			7.08			0.86					
from kinetic energy from g (‰)	8.77			2.51			1.44			6.06			7.10			0.87					

Figure 1: (a) SEM micrograph (BSE mode) of a section of a recovered ^{57}Fe-doped olivine single crystal. The lighter grey upper part of the crystal was in contact with the isotopically labelled FeO-MgO oxide mixture during thermal annealing. It was therefore slightly enriched in FeO and labelled in ^{57}Fe. The small white zones present around the crystal (mainly on the left upper surface) are small patches of this oxide mixture. This indicates imperfectly prepared samples. In this case, additional grinding was preformed to remove any trace of such oxide mixture. (b) Experimental setup used during HT in-situ NRIXS measurements (see text for details).

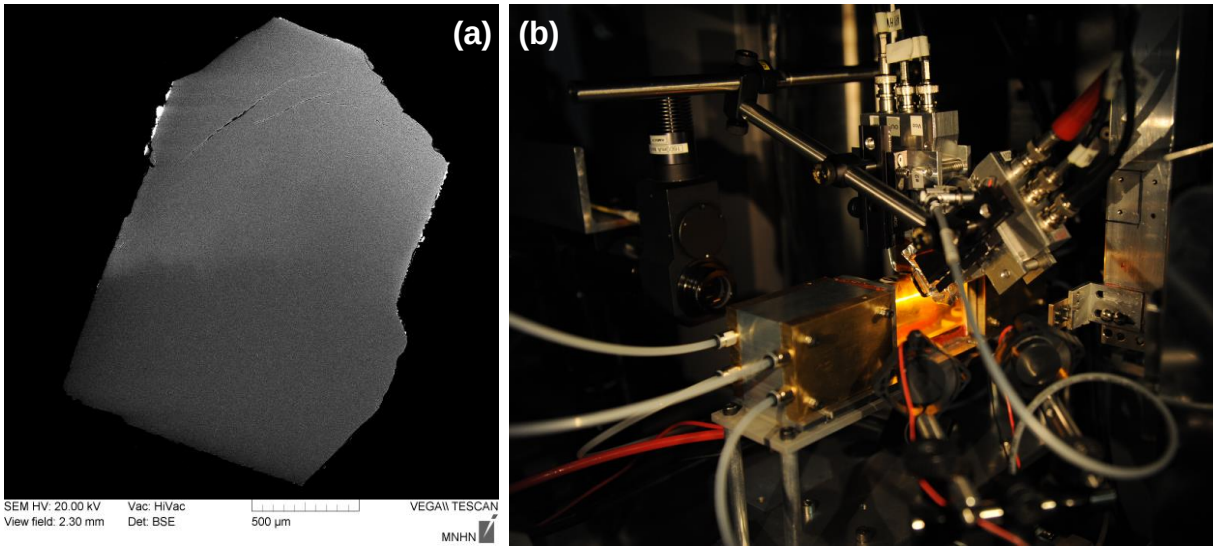

Figure 2: Mössbauer spectra of simplified glasses and natural analogs. The data collection was carried out at temperature varying from 5K to 300 K.

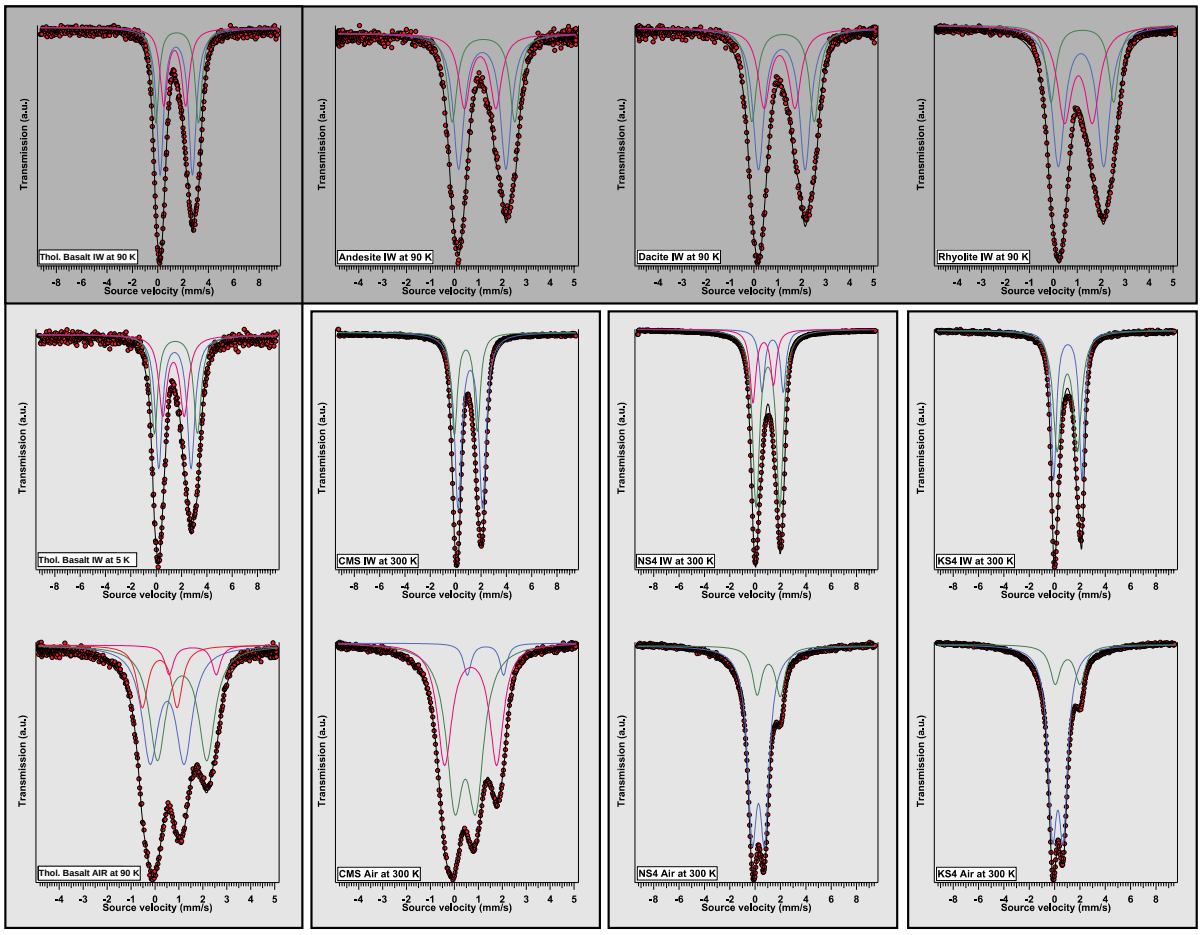

Figure 3: Partial density of states of simplified glasses collected at room temperature and presented against spectra collected on glasses of natural compositions (From Dauphas et al., 2014).

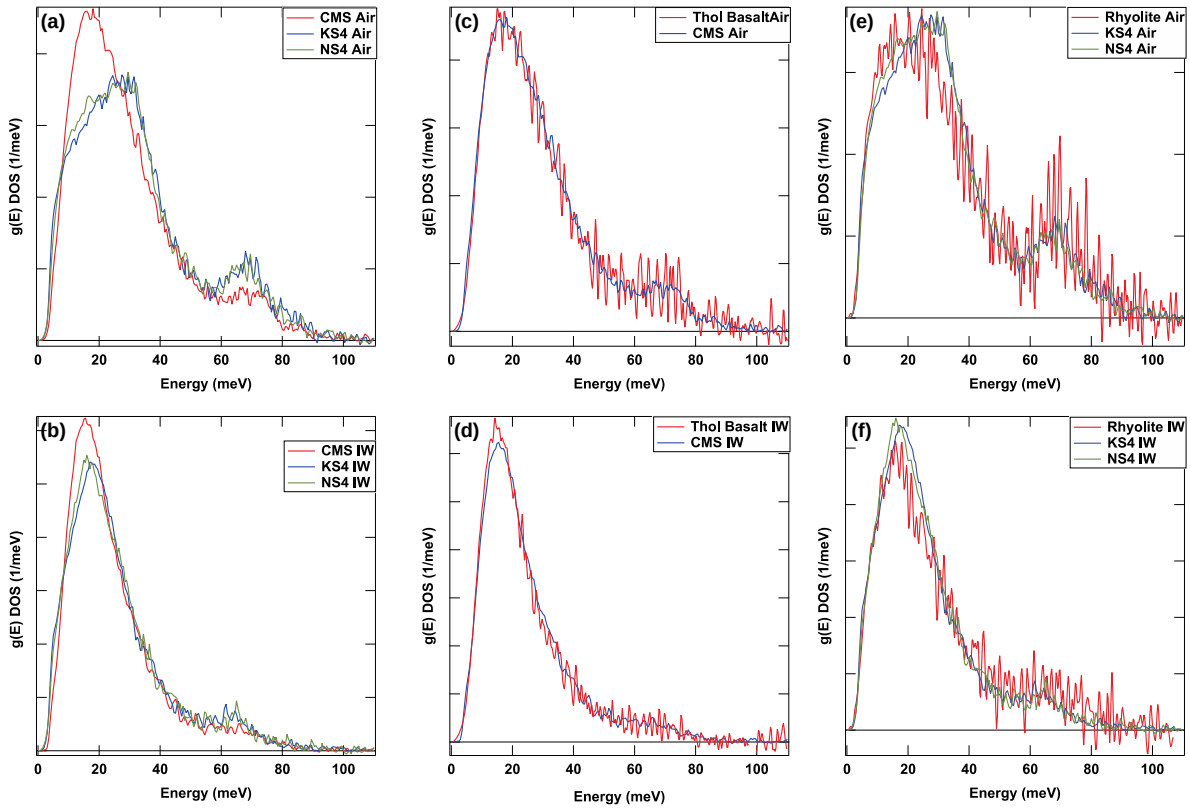

Figure 4: Inverse of Lamb-Mössbauer factor of studied glasses derived from NRIXS spectra as a function of the fraction of the Mössbauer peak surface area that can be ascribed to Fe^{3+} divided by the total Mössbauer peak [$S_{Fe3+}/S_{tot}= S_{Fe3+}/(S_{Fe3+}+ S_{Fe2+})$]. The errors of $1/f_{LM}$ are smaller than the data points and hence not plotted in the figure.

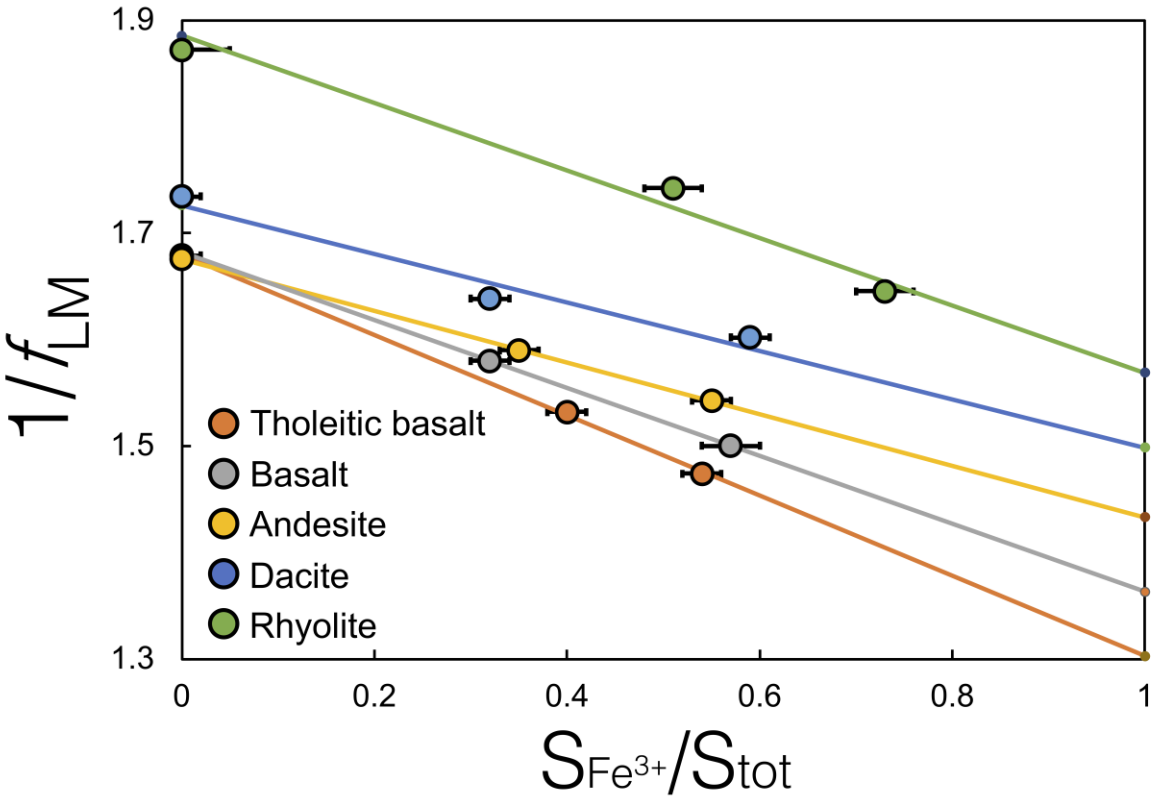

Figure 5: Iron PDOS of basaltic glass synthesized in air and olivine at 300, 558, and 773 K. The PDOS of the basaltic glass remains completely unchanged when the temperature increases. The PDOS of the olivine crystal differ between the different temperature acquisitions but this most likely reflects differences in crystal orientations between the runs rather than true changes in the PDOS with temperature. Note that one olivine crystal was measured at 1223 K but the Lamb-Mössbauer factor was low (~0.226) and as a result, the calculated PDOS shows large negative excursions and is unreliable. For that temperature, we therefore only report data that we deem to be reliable (Table 5).

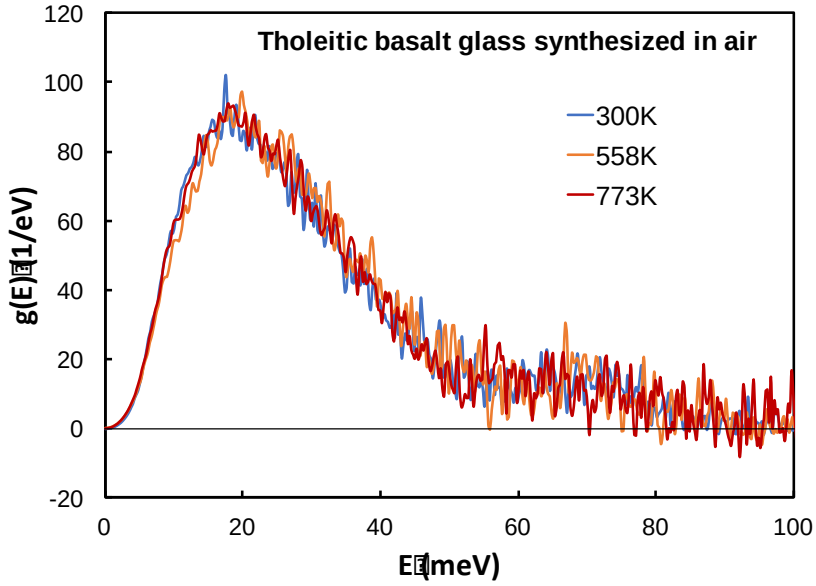

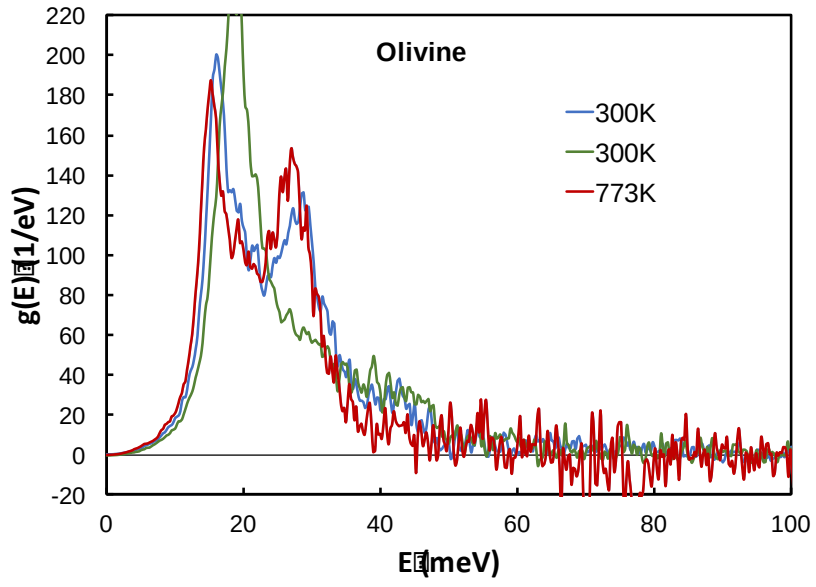

Figure 6. Assessment of the harmonicity of iron bonds in basaltic glass (red filled circles) and olivine (orange filled circles). The green filled circle correspond to a second spectrum of olivine collected at ambient condition but in a very different orientation (See fig. 5). If the interatomic potential departed significantly from harmonic behavior, we would expect the force constant of iron bonds to change as the temperature and mean square displacement increase. For a quartic potential, the correlation would be linear (see text for details). As shown, the slope of the correlations defined by the data points are zero within uncertainties (-568±3045 for olivine; -4865±4662 for basaltic glass), meaning that the data are close to harmonic up to the temperatures of 773 K investigated. Therefore, it is justifiable to use force constants measured at room temperature to calculate the equilibrium isotopic fractionation of iron in metamorphic rocks and possibly igneous rocks. Further work is needed to test whether structural changes in liquids or anharmonicity in liquid/solid in the solidus/liquidus region induces changes in iron bonds relative to glasses.

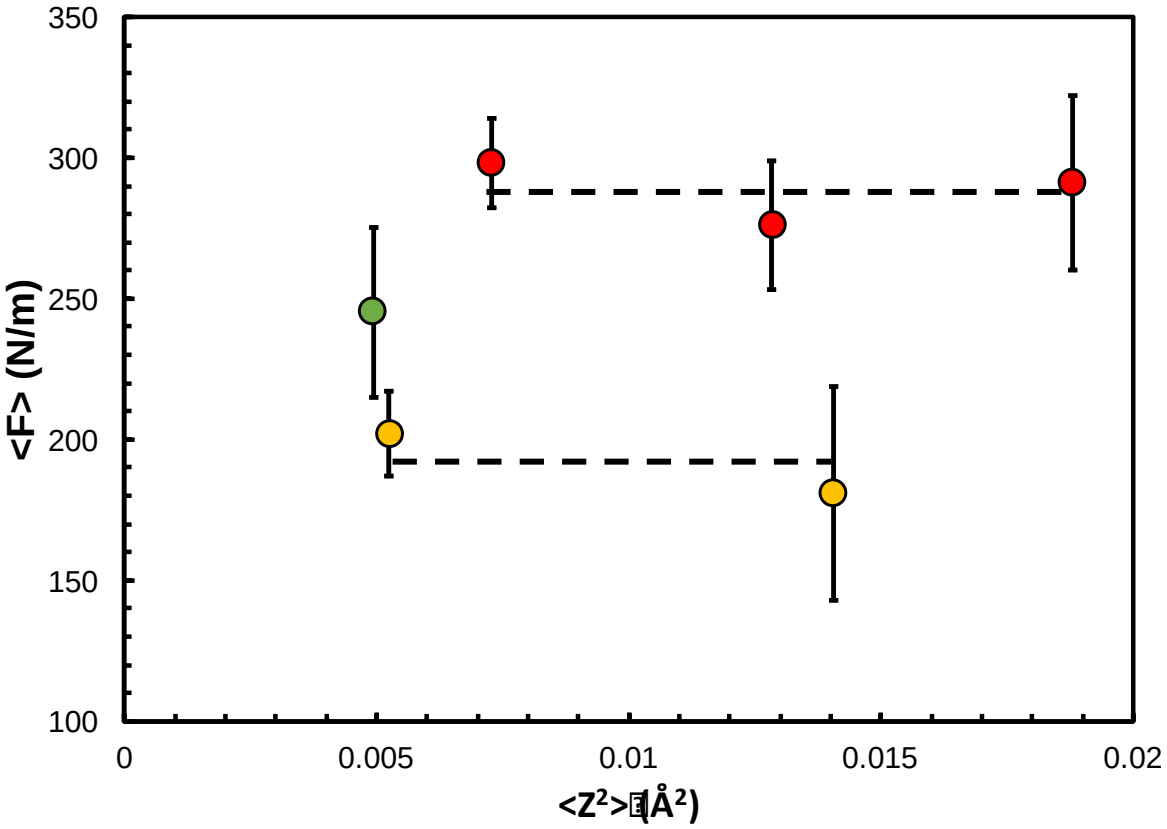

Figure 7: Values of ln*C* as a function of temperature for Tholeitic basalt, basalt, andesite, dacite, and rhyolite. The dashed line is the average of ln*C* of all five glass compositions. (b) Lamb-Mossbauer factor of basalt (grey) and olivine (red) as functions of temperature. The points are experimental determinations of Lamb-Mossbauer factors at certain temperatures and the curves predict the variation of Lamb-Mossbauer factors as a function of temperature based on PDOS of the basalt and olivine at room temperature. The olivine datum at 1223 K is discrepant as explained in the text, and was discarded.

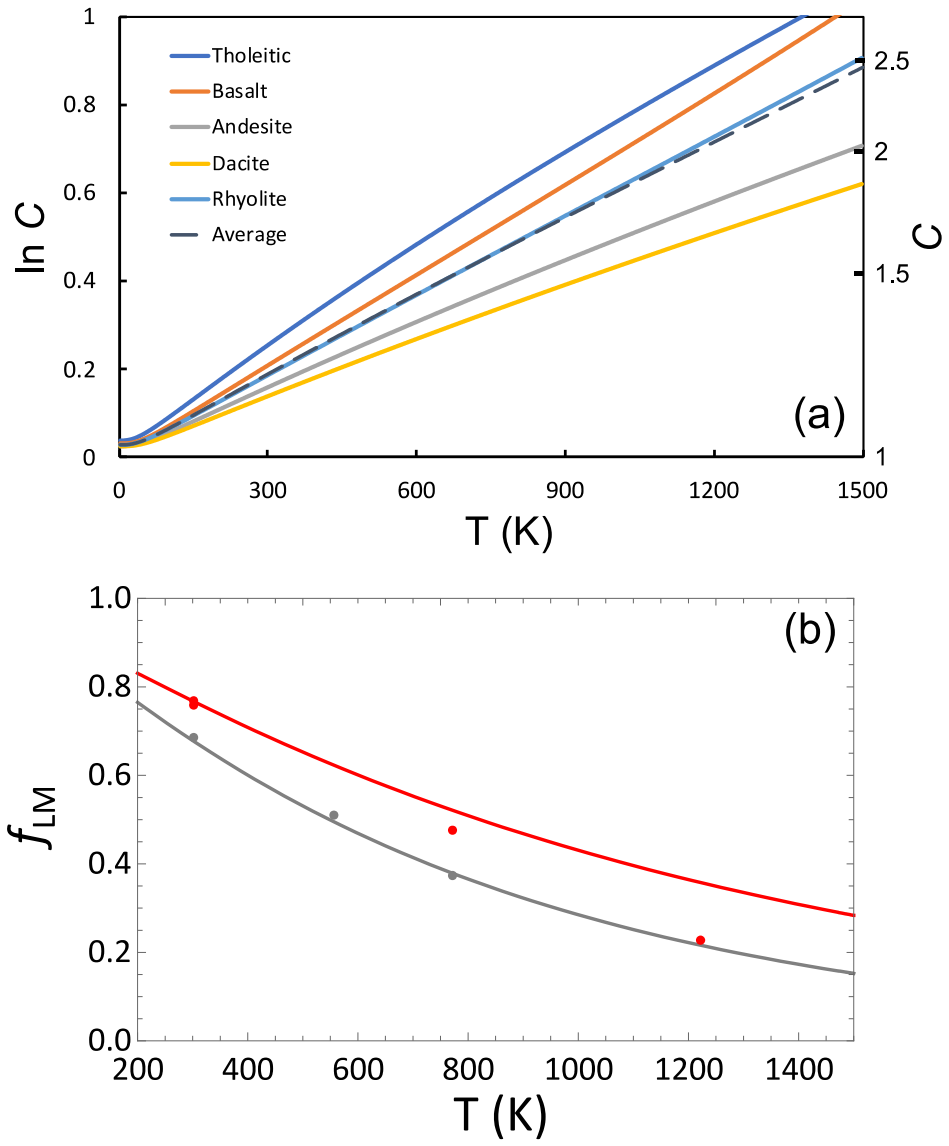

Figure 8: Data compilation of rescaled energies of the centroid of the pre-edge feature as a function of the corrected redox ratios determined by Mössbauer spectroscopy. Presented data are for basalts, andesites, dacites and rhyolites published in Cottrell et al. (2009), Dauphas et al., (2014), Zhang et al. (2015-2016), Fiege et al. (2017, here only data collected at APS for simplicity, data from ANKA being consistent but shifted in energy as explained by authors) and Berry et al., (2018). In all cases, uncorrected redox ratios were used. A uniform correction using our average C-value of 1.196 was then applied to all Mössbauer data. The energies of the centroid provided by Berry et al. (2018) and by Fiege et al. (2017) were empirically rescaled such that basaltic glasses from the different studies exhibiting similar Mössbauer-derived redox ratios plot on a single line. In practice, a constant correction of +1 eV was applied to the dataset of Berry et al. (2018) and of +0.46 eV to the dataset of Fiege et al. (2017). No further correction had to be applied to account for compositional variations among basalts, andesites, dacites and rhyolite. Data for rhyolites are from Cottrell et al., (2009), Dauphas et al., (2014) and Fiege et al., (2017). A typical error of ±0.022 eV for the centroid energy and 0.02 for the redox ratios determined by Mössbauer spectroscopy are reported here. Parametric fits to the data have the form: $\Delta E = -0.82 \cdot (\mathrm{Fe}^{3+}/\Sigma\mathrm{Fe})^2 + 1.97 \cdot (\mathrm{Fe}^{3+}/\Sigma\mathrm{Fe}) + 7112.39$ for the rhyolites and $\Delta E = -1.19 \cdot (\mathrm{Fe}^{3+}/\Sigma\mathrm{Fe})^2 + 2.75 \cdot (\mathrm{Fe}^{3+}/\Sigma\mathrm{Fe}) + 7212$ for other compositions. These fits take into account the physical limitations provided by Westre et al. (1997) and Wilke et al. (2007) and therefore, the trend of centroid end at ca. 7112 eV as observed on Fe^{2+} model compounds and in accordance with multiplet theory as well as crystal field splitting by optical spectroscopy.

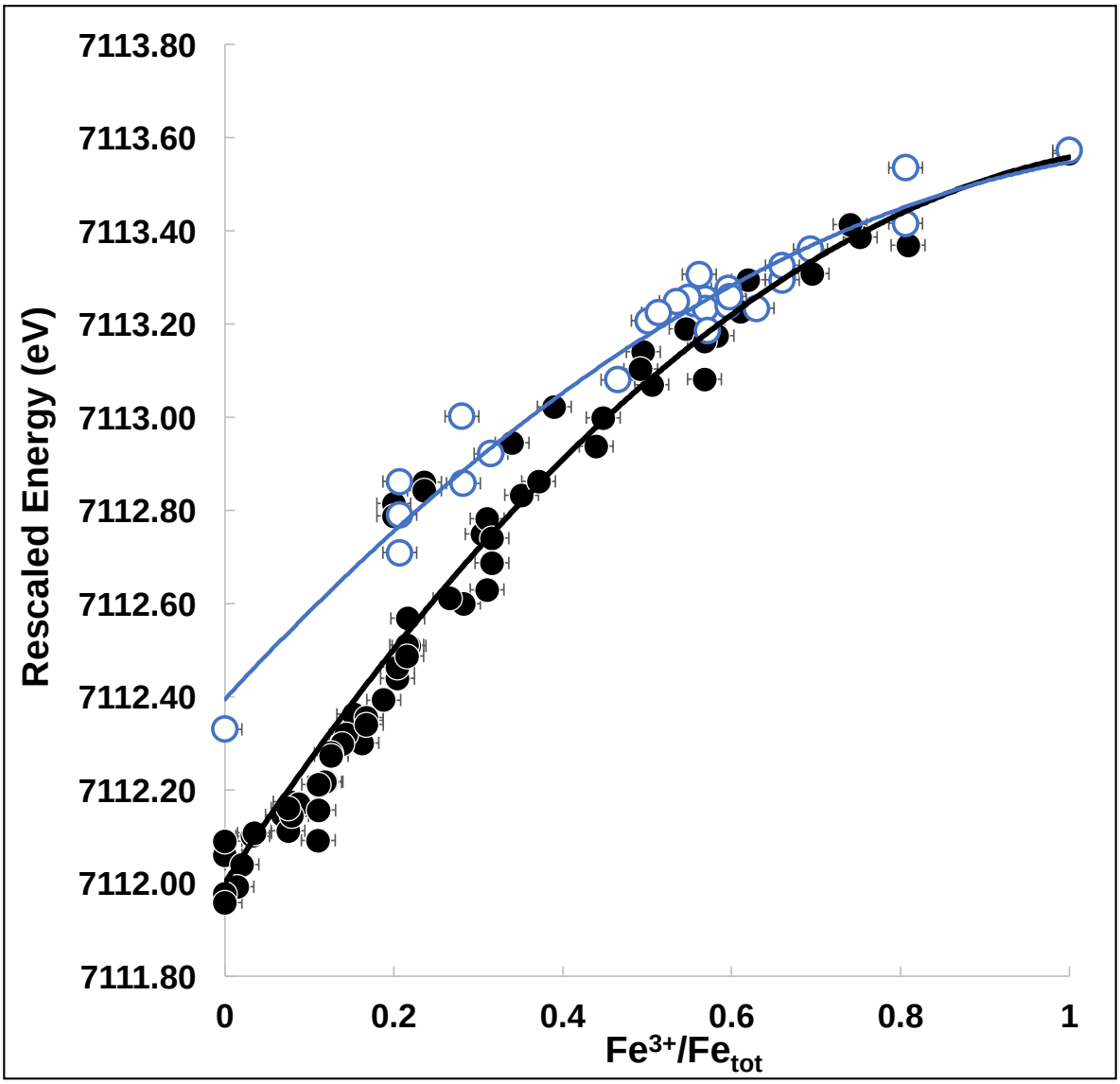
7113.80
7113.60
7113.40
7113.20
7113.00
7112.80
7112.60
7112.40
7112.20
7112.00
7111.80
Rescaled Energy (eV)
0
0.2
0.4
0.6
0.8
1
Fe3+/Fetot

1182

1183

Figure 9: Reappraisal of the iron force constants in variably oxidized synthetic silicate glasses (Dauphas et al., 2014). Basalt, andesite, dacite, and rhyolite glasses define linear arrays that can be extrapolated to $Fe^{3+}/\Sigma Fe = 0$ and $Fe^{3+}/\Sigma Fe = 1$ to estimate the force constants of Fe^{2+} and Fe^{3+}, respectively. Basalt, andesite, and dacite define a single correlation that gives force constants of 193 ± 7 and 364 ± 23 N/m for the Fe^{2+} and Fe^{3+} end-members, respectively. Rhyolite defines a different correlation that gives force constants of 250 ± 11 and 382 ± 31 N/m for the Fe^{2+} and Fe^{3+} end-members, respectively. The regressions were calculated using the Isoplot software. Uncertainties are 95% confidence intervals. Data for simplified glasses also demonstrate that potassium (and sodium to a lower extent) has a strong effect on the force constant of Fe^{2+}.

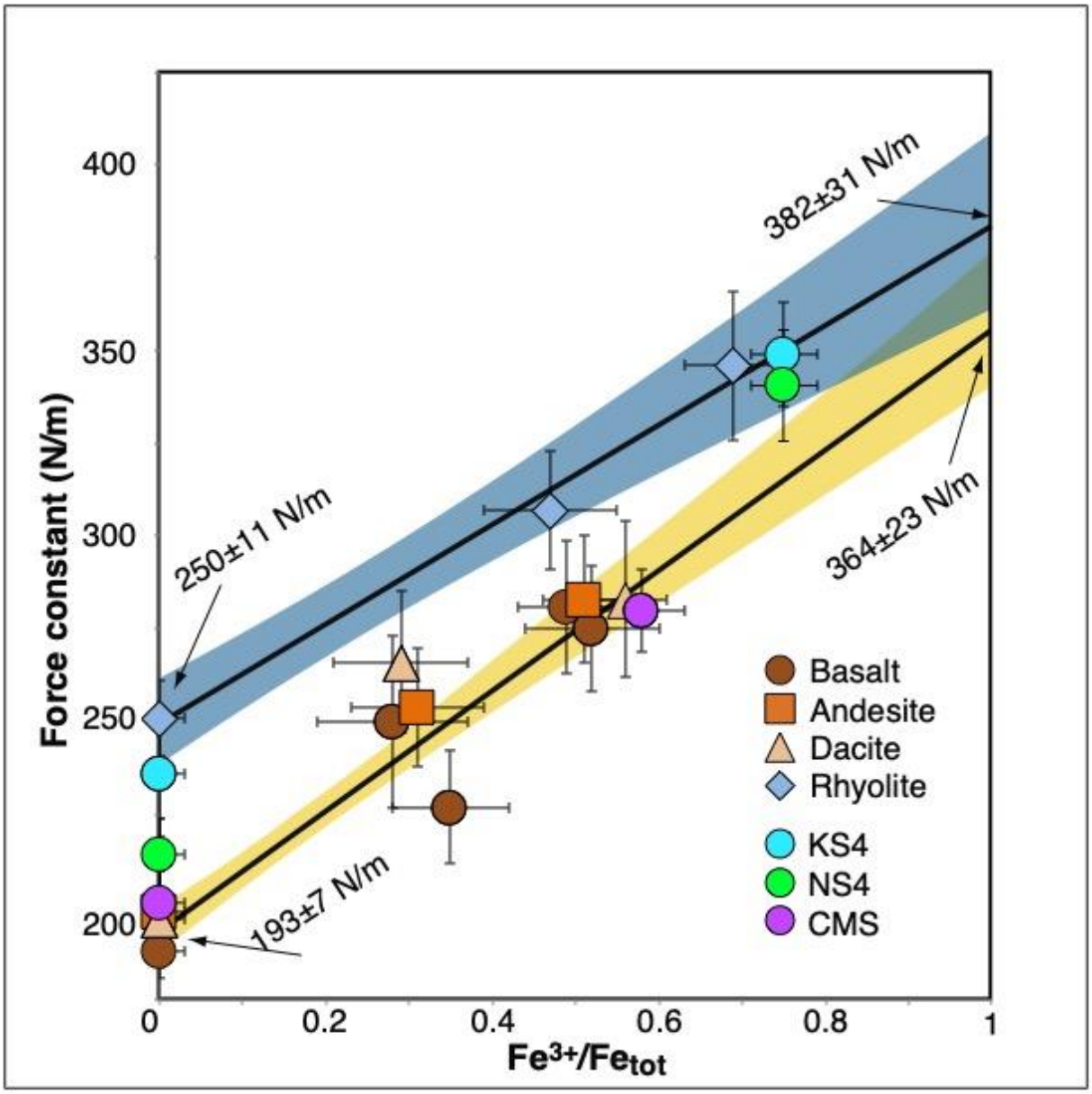

Figure 10: Mössbauer parameters (Isomer shift, IS and Quadrupole splitting, QS) for reduced glasses. Fit to the data were performed with three Lorentzians. These three lines define three clusters of parameters. In each cluster, data define trends from basalt to rhyolite (from high IS-QS to low IS-QS). The effect of acquisition temperature is also seen for the basaltic glass for which data were collected at 5 and 90K.

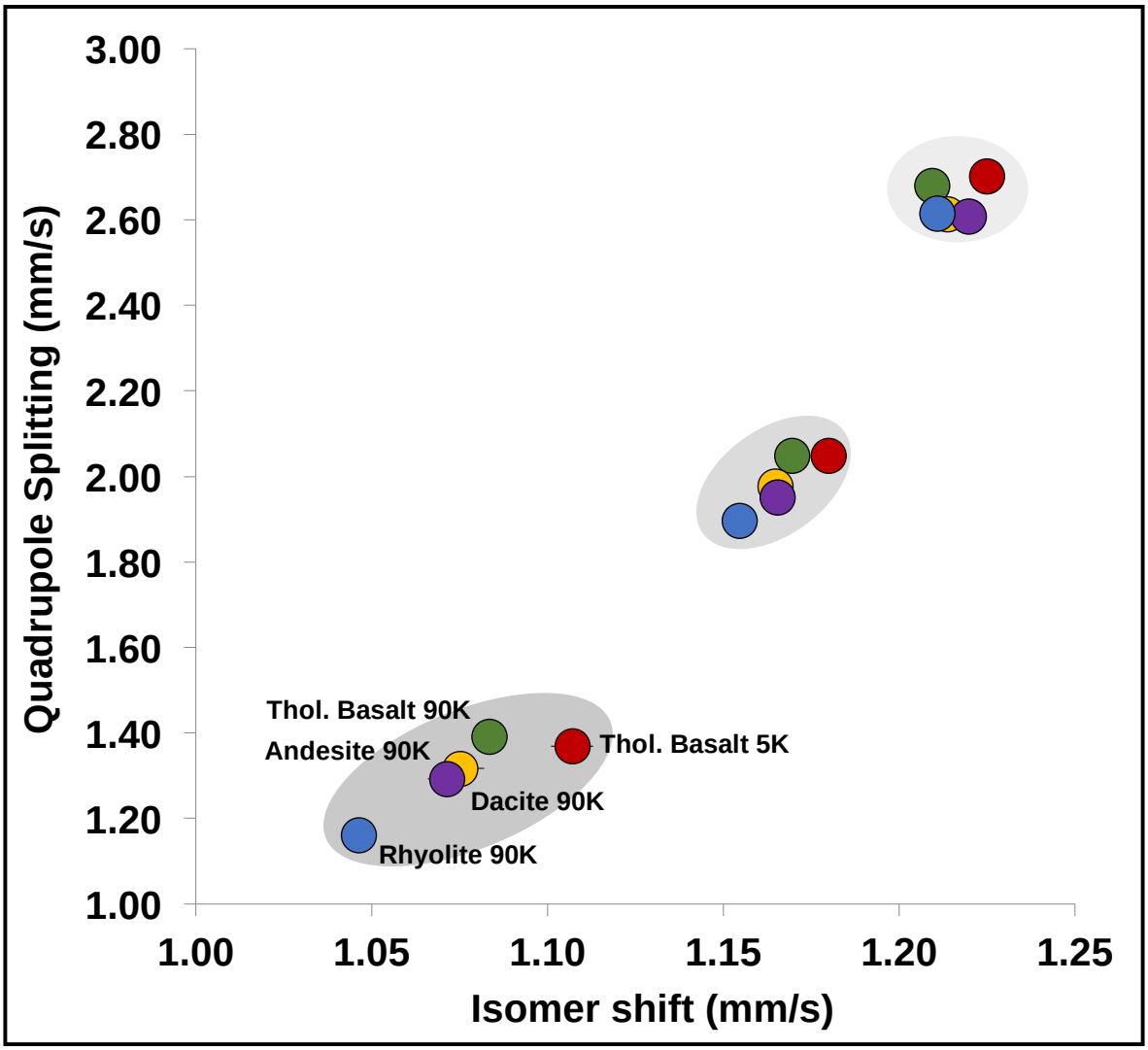

Supplementary material: Compositional (sensu latto) dependences of f_{LM} and <F>.